To the Graduate Council:

I am submitting herewith a thesis written by Richard Collier entitled "Characterization of a Range Scanning System Utilizing a Point Laser Rangefinder." I have examined the final copy of this thesis for form and content and recommend that it be accepted in partial fulfillment of the requirements for the degree of Master of Science, with a major in Electrical Engineering.

R. T. Whitaker, Major Professor

We have read this thesis
and recommend its acceptance:

Accepted for the Council:

Associate Vice Chancellor
and Dean of The Graduate School

CHARACTERIZATION OF A RANGE SCANNING SYSTEM UTILIZING A POINT LASER RANGEFINDER

A Thesis

Presented for the

Master of Science

Degree

The University of Tennessee, Knoxville

Richard Collier

August 1998

ACKNOWLEDGMENTS

I would first like to thank my parents, Tom and Monica Collier, for their support and continuous encouragement throughout my educational career. I would also like to extend thanks to my sister and her family for their high expectations. My sincere gratitude goes out to Amy for her endless patience and devotion during times of frustration. Thanks to Dr. M. A. Abidi and Dr. R. T. Whitaker for their guidance throughout my research program. Finally, thanks to the members of my committee, Dr. R. T. Whitaker, Dr. M. A. Abidi, and Dr. J. Gregor for their help and constructive criticism.

The work in this thesis was supported by the DOE's University Research Program in Robotics (Universities of Florida, Michigan, New Mexico, Tennessee, and Texas) under grant DOE–DE–FG02–86NE37968.

ABSTRACT

This thesis presents an error characterization scheme with application to a pulsed time-of-flight laser rangefinder called the AccuRange 3000. Characterizations of range-imaging sensors are important because they determine the limitations of the sensor. Also, characterizations are the first step in developing a correction model for range data and they provide information about the amounts of error present in the data to aid in post-processing techniques. The combination of all these factors provide a basis for making a decision on which type of sensor to use for a particular application. First, the thesis reviews range imaging sensor technology. This review is followed by a discussion of previous work in the areas of characterization of laser rangefinding systems and error models of laser rangefinders. A technical description of the pulsed time-of-flight laser rangefinder coupled with the mechanical scanning system we use for data acquisition is given. Also, this thesis details a simulation of the entire system developed using Telegrip simulation software. The thesis gives an error characterization of the laser rangefinder utilized as a point laser. This includes errors associated with temperature, sampling rates, mixed pixels, varying values of reflectance at incremental distances and varying values of reflectance at incremental angles of incidence. Selected information gathered during these experiments are combined to form a correction model of the laser system. This correction model is based on the range and intensity data output from the laser rangefinder. A comparison of corrected and uncorrected range values is given for several data sets. Also, a confidence metric is derived and given for each corrected range value. The confidence metric is an estimation of how much error is present in the corrected value. The thesis concludes with a discussion of the results and possible extensions for future work.

Contents

List of Figures

CHAPTER 1

Introduction

1.1 Problem Statement

Range determining sensors have been around for over thirty years. With the advancement of technology, these sensors have developed into compact systems that are deployed in many different situations. Manufacturing and robotics have both taken advantage of 3-D sensing technology.

With the ever increasing competitiveness of the business world, manufacturers look for ways to automate their processes in order to reduce costs and protect workers from possible injuries. Range sensors can help achieve automation by providing information about the 3-D structure of a product during various phases of manufacturing. Often range sensors are used in the quality control phase of the manufacturing process. They provide real time information about a product's shape and size which can be used as feedback for process control or as a method for rejecting substandard products.

The manufacturing industries were also one of the first to take advantage of robotic technology. Robots are able to handle the repetitive tasks often found in the manufacturing process and operate with a predetermined program controlling their moves. With the advancement of range sensors, robot technology is able to break away from the carefully controlled environments of the manufacturing settings and use data collected from these sensors to operate more flexibly with less human oversight or control. Robots that operate without human intervention are called autonomous. Autonomous robots have the a wide range of potential applications including hazardous waste clean-up and mobile mapping.

For autonomous robots or inspection systems to perform correctly, the range sensors have to operate to a certain degree of accuracy and precision. The limits of how well these systems perform is directly related to how well the range sensors perform. Therefore, the dependence on sensors is critical. Knowledge of how these sensors work and their limitations is a major concern in selecting the proper sensor for a particular application.

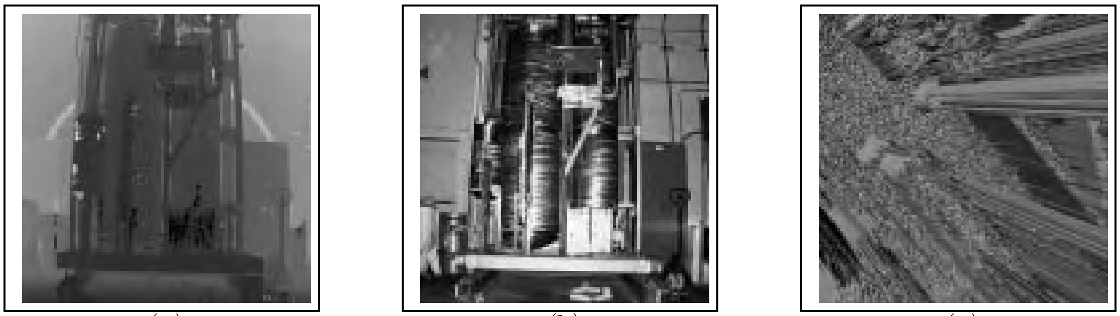

(a) (b) (c)

Figure 1.1: *(a) A range image of a typical scene found in the area of waste disposal. (b) An associated amplitude image of the same scene. (c) A close up of the range data plotted in 3-D.*

Figure 1.1 shows a range and associated amplitude image taken with the Perceptron laser range scanner along with a 3-D plot of some of the range data. The object in the image represents a typical scene often found in contaminated facilities that need to be dismantled and disposed of properly. The data does not appear at first glance to be very noisy in the range image, but the three dimensional plot shows otherwise. This scanner as it stands would not be a good candidate for guiding a robot's arm to specific parts in the scene because of the noise present in the laser range system. What applications could this scanner be applied to? The answer to this question depends upon the accuracy needed for the application. How accurate is the scanner? How precise is the scanner? What variables cause degradation in the sensor's measurements? These are all questions that need to be answered so the limitations of the scanner can be established.

One way to determine the limitations of a sensor is to characterize its performance. Characterization is the process of experimentally and/or theoretically determining the factors that affect the quality of the sensory data. By identifying and quantifying these factors, viable applications for the range sensor can be decided. Also, this process precedes the development of a correction model for the sensor which can be used for correcting the degrading factors. The identification process and the resulting correction model is the focus of this thesis.

1.2 Strategy

This thesis presents a characterization of a pulsed time-of-flight laser rangefinder used to acquire range and associated amplitude images. Some research has been done on sensor characterization, however, characterizations need to be performed on a per system basis because of irregularities in device electronics and mechanical variations. This thesis makes contributions in the areas of laser rangefinder characterization and error modeling from a *black-box* perspective. By not focusing on the internal structure of the sensor, it allows the sensor to become an interchangeable part of the system while the characterization technique remains the same.

Our method looks at operational parameters and conditions first. We examine how the input parameters such as sampling rate and resolution affect range measurements. Also, we look at how temperature affects range measurements. This includes environmental temperature as well as device electronics temperature. After we have examined the initialization variables, we use the results from these tests to determine our parameters for taking data. Secondly, we look at how mixed pixels, variations in reflectance, and angle of incidence corrupt the range data. Our tests use multi-colored, matte surfaces at incremental distances to determine the error in the range measurements due to these effects.

With the identification of all relevant sources of error in the laser system, we begin the development of our correction model. We use a plane that is made up of grayscale values that increment from white to black. We scan this plane with our range imaging system at several distances. These distances represent the operational range of the system. The laser returns two values, the range and the amplitude of the signal returned. We define the amplitude of the signal returned as the *intensity*. By calculating the error in the range measurements and plotting the error versus the range and intensity, we have a surface that represents the error in our scanner. We use a least squares approximation to fit a surface to the plot of the error to generate our correction model. By using the algorithm generated by the least squares approximation, we can correct the range data to improve the accuracy and precision of our laser range scanning system.

We then apply the correction algorithm to our original data taken of the plane at several distances. Once again, we calculate the error. We plot the squared error of the corrected data versus the original intensity. We then use the same method to fit a surface to the squared error. This gives an algorithm to estimate how much error will be present in the range data after the correction algorithm is applied. This is our error model or confidence metric for our sensor.

The development of both of these algorithms gives us a better understanding of the capabilities of our scanning system. The correction algorithm improves the accuracy and precision of the range measurements while the confidence algorithm provides us information about the corrected data that is useful for many post-processing techniques.

1.3 Overview of Thesis

The remainder of this document is as follows. Chapter 2 is a review of range-imaging techniques, similar work in sensor characterization and error modeling. Chapter 3 discusses the design of our scanning system from a hardware and software perspective. In addition, it describes the different modes of operation for taking range data and contains a simulation model of our system.

Chapter 4 begins by detailing some initialization effects caused by temperature, operating parameters of the laser, and device electronics. Then it examines the effects of mixed pixels, color, and angle of incidence in different modes of operation. Also, it describes the process of developing a correction algorithm by modeling the inconsistencies of the laser and shows the results generated by this method. Then a confidence measure in the corrected data is calculated and discussed. Finally, chapter 5 gives our conclusions about our work in laser rangefinder characterization and modeling with suggestions for improving our technique.

CHAPTER 2

Background Section

There are several classes of range-imaging devices. The following sections give a breakdown of commonly used range-imaging techniques and discusses their limitations.

2.1 Range Data Acquisition Methods

The majority of the devices used for robotic sensory applications are direct measurement systems. Direct measurement sensors result in range measurements i.e., the distances between a range sensor and a set of surface points in a scene of unknown properties. There are two types of direct measurement strategies: triangulation methods and time-of-flight methods. Figure 2.1 gives a taxonomy of direct measurement 3-D imaging techniques. Theoretical aspects of each of the techniques in the figure and limitations will be examined in later sections.

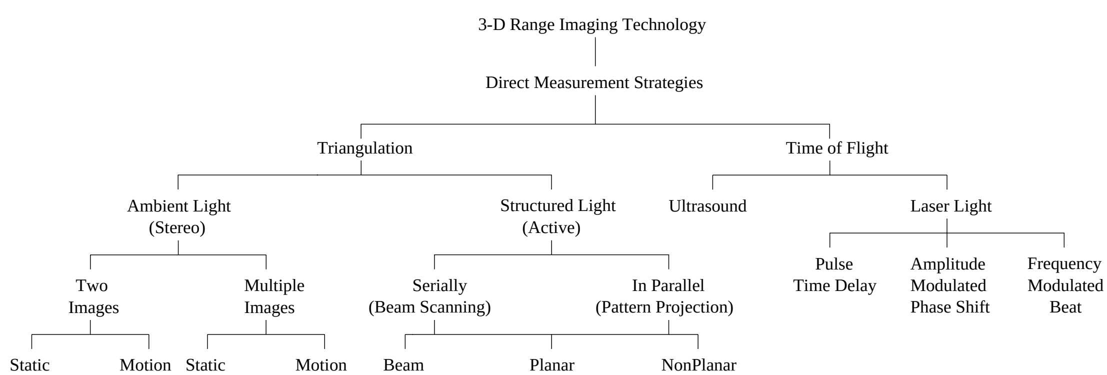

Figure 2.1: *Techniques for measuring three-dimensional data. Adapted from [1].*

Indirect measurement systems are also available. They infer distance or surface orientation from monocular images on the basis of target properties. Some examples of indirect measurement techniques are range from focusing, range from known geometry, range from shadows, and range from Moirè fringe patterns. Indirect systems are not yet widely used in applications and are outside the scope of this thesis.

2.1.1 Stereo Imaging and Structured Light

Triangulation methods are based on elementary geometry. Given the *baseline* of a triangle, i.e., the distance between two of its vertices and the angles at these vertices, the range from one of the vertices to the third one is computed as the corresponding triangle side. Figure 2.2 illustrates this process. Stereo imaging is perhaps the most well known triangulation method; it is based on human vision. Stereo uses an imaging sensor (usually a CCD camera) at each of the two triangle vertices. A pair of images is obtained from both vertices. The projections of a point are located in both images and the range to the point is computed using the geometric method previously described. Structured lighting replaces one of the imaging sensors utilized in stereo with a controlled illumination source. The illumination source is usually a laser which projects a line of light onto a scene that is captured by the remaining imaging sensor and range is derived in the same manner [1].

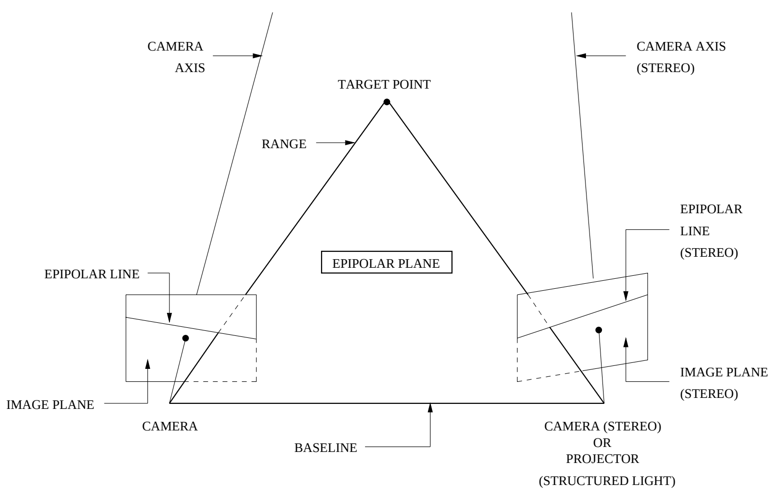

Figure 2.2: *Range sensing by triangulation. Adapted from [1].*

A significant problem with virtually any triangulation technique is *missing data* for pixels in the scene that are not "seen" by both imaging sensors at the vertices of the triangle. Another limitation of triangulation techniques is the baseline. In order to scan areas larger than a couple of square meters, a baseline of a few meters or more will be needed. This introduces the problem of maintaining a rigid reference frame between the two sensors [2].

Passive stereo also has the problem of matching corresponding points in both images reliably and quickly. The correspondence problem is ill posed and has evaded a reliable, accurate solution. The existence of the illumination source for structured light helps with the correspondence problem, but introduces specular reflections. Specular reflection is the effect of light scattering on shiny surfaces that may result in no range measurement if the reflected light does not reach the camera. Specularities can also generate false measured range values if the reflected light is subsequently reflected by other surfaces before part of it reaches the camera [3].

2.1.2 Time-of-Flight Techniques

Time-of-flight techniques are so named because they use a signal transmitter to send a signal to a target while a detector collects the reflected signal. The range, r, is given by

$$r = \frac{v \triangle t}{2} \tag{2.1}$$

where v is the speed of light/sound and $\triangle t$ is the total time it takes the signal to travel the total distance. There are several variations on this theme that use different energy sources and different output/input signals.

Ultrasound Imaging

Ultrasonic rangefinders are an example of a time-of-flight system. An ultrasonic rangefinder uses a sound transducer for both the transmitter and receiver. When in the transmitting mode, the transducer generates a short burst of sound. When in the receiving mode, the transducer acts as a microphone with range being determined by measuring the time interval between the transmitted pulse and the returning echo.

Due to great difficulty in generating a narrow acoustic beam, ultrasonic range-imaging systems suffer from low resolution and are therefore limited in range image acquisition applications. Ultrasound, as well as most other active sensing strategies, relies on Lambertian reflection of the incident signal and may malfunction if the target surface is too glossy or shiny [1].

Amplitude-Modulated Laser Rangefinders

Laser rangefinders also operate by time-of-flight. Laser rangefinders use time delays of reflected beams to infer distance. They can be roughly divided into two classes depending on whether their light emission is continuous or pulsed. Continuous laser rangefinders operate on the principle of emitting a continuous beam and inferring range as a function of the phase shift between the outgoing and incoming beams. A subset of continuous-wave laser rangefinders is amplitude-modulated (AM) systems.

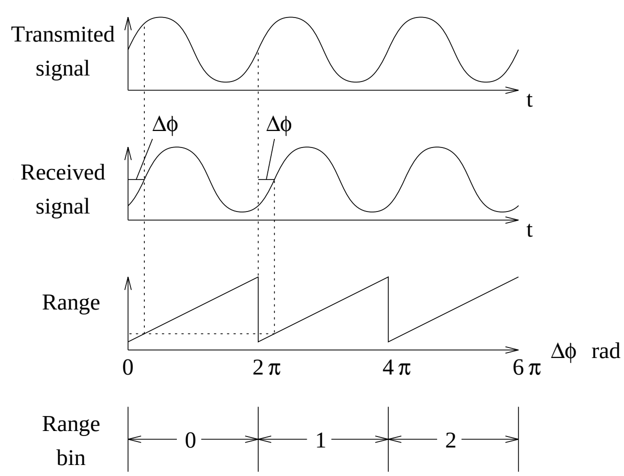

Figure 2.3: *Range as a function of phase shifting for an amplitude-modulated continuous wave laser range finder. Adapted from [4].*

An AM laser rangefinder modulates the amplitude of a laser beam (Figure 2.3) at a frequency $f_{AM} = c/\lambda_{AM}$ where c is the speed of light and λ_{AM} is the wavelength of laser.

By measuring the phase difference between the incoming and outgoing signal:

$$\triangle\phi = 2\pi f_{AM} \triangle t = 4\pi f_{AM} \frac{r}{c}, \tag{2.2}$$

range is computed [5] according to

$$r(\triangle\phi) = \frac{c}{4\pi f_{AM}} \triangle\phi = \frac{\lambda_{AM}}{4\pi} \triangle\phi. \tag{2.3}$$

A problem involving AM laser rangefinders is evident when the range values exceed the ambiguity interval of $\lambda_{AM}/2$. This causes equivocal range measurements because it is impossible to determine the period in which the phase shift occurs.

Frequency-Modulated Rangefinders

Another type of continuous-wave laser rangefinder is frequency-modulated (FM). In an FM system, the optical frequency of a laser diode can be tuned thermally by modulating the laser diode drive current. If the transmitted optical frequency is repetitively swept linearly between $(v - \triangle v/2)$ and $(v + \triangle v/2)$ creating a total frequency deviation of $\triangle v$ during the period $1/f_m$, the reflected return signal can be mixed coherently with a reference signal at the detector [6]. The mixing of the return signal and the reference signal produces a beat signal [7]. This coherent mixing is often a multiplication of the reference and return signals. The beat signal is demodulated to produce a beat frequency, f_b, which is a periodic waveform. The beat frequency is proportional to the number of zero crossings in one ramp period.

The range is determined from the following equation [6]

$$r(f_b) = \frac{cf_b}{4 f_m \triangle v}. \tag{2.4}$$

The absence of phase measurement in this system precludes the possibility of an ambiguity interval. Figure 2.4 illustrates this principle.

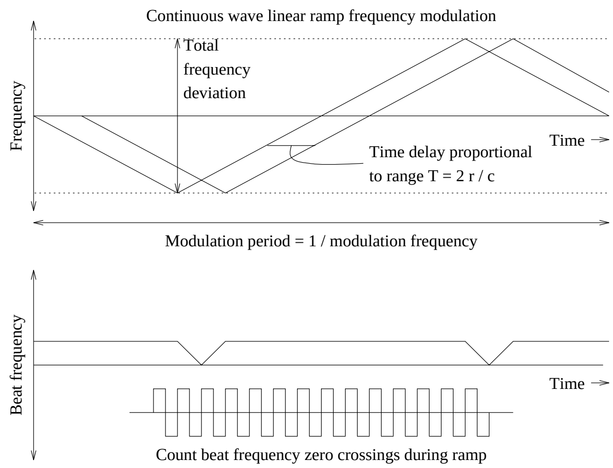

Figure 2.4: *Frequency modulated continuous wave radar principles. Adapted from [6].*

One of the major sources of noise in FM laser rangefinders is *speckle*. Speckle effects originate from surface roughness at the microscopic level and is therefore related to properties of the material being scanned. When illuminated by a coherent wavefront of light, reflections tend to be out of phase, giving rise to random constructive and destructive interference which results in a specular looking reflection [5].

Pulsed Laser Rangefinders

In the pulsed rangefinding method, the distance is obtained by measuring the time interval between a *start pulse* and a *stop pulse*. The start pulse is obtained from the transmitted signal and the stop pulse from the received signal which is reflected and detected. The detection of the stop pulse is used as a trigger for successive pulses which generates a pulse repetition rate at frequency f_p. The range is inversely proportional to f_p: [8]

$$r_m = \frac{c}{2f_p}. \tag{2.5}$$

Pulsed laser rangefinders also suffer from the effects of speckle. The same type of random constructive and destructive interference appears in the returned signals.

2.1.3 Known Problems with Laser Rangefinders

There are some common problems that impact virtually all laser rangefinders. Among these are *mixed pixels*, *angle of incidence*, and *reflectivity*. The mixed pixel phenomenon occurs when the footprint of the laser falls on the edge between two surfaces which are located at different distances. The fact that the range is measured by integrating over the entire projected footprint may produce phantom objects due to mixed measurements that are inaccurate [9]. A diagram which illustrates this phenomenon at the signal level of an amplitude-modulated ranging system is shown in Figure 2.5.

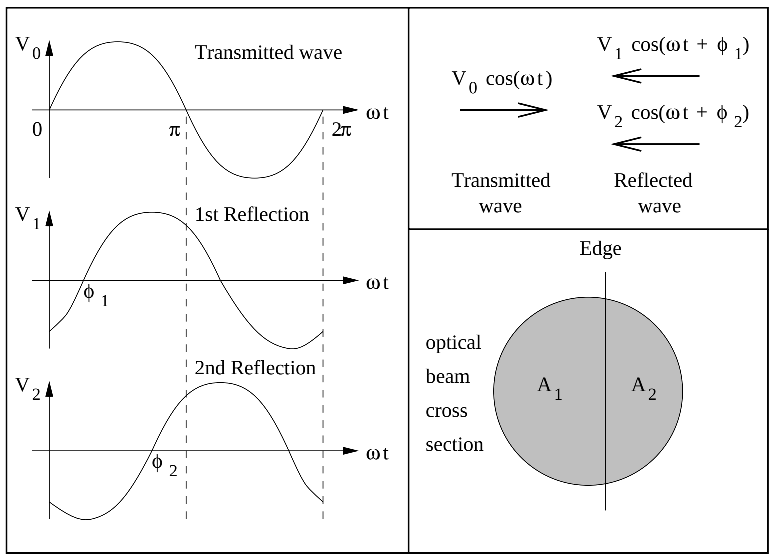

Figure 2.5: *The transmitted signal of an Amplitude-Modulated Continuous Wave laser radar is split into two signals of differing phase by an edge. This effect is commonly known as the mixed pixel effect. Adapted from [10].*

The angle of incidence between the emitted light beam and the target surface also introduces inaccuracies. As the angle of incidence increases, the area of the laser footprint increases. As the area of the footprint increases, the precision of the range measurement degrades. This is because of reduced energy being reflected back along the collimated beam of light onto the detector [11].

Ideally the reflective property of the material being scanned should have no effect on the range measurement, but this is not the case. Because light is the driving force behind laser rangefinders, the reflectance characteristics of the target does have an effect on the accuracy of the measurement value. Most laser rangefinders are calibrated to work in an optimum range of reflectance values such that only the extreme ends of the range presents significant problems. This means that inaccurate range measurements are produced by very dark objects because less of the signal reaches the detector and highly reflective objects produce inaccurate range measurements because they tend to saturate the detector.

2.2 Review of Work on Sensor Characterization and Modeling

Despite the broad expanse of range-imaging systems available today, there is only a modest amount of research being done on sensor characterization. Instead, manufacturer specifications are often accepted as a working description of a system. We shall show in this thesis that manufacturer specifications are not always an accurate depiction of a system's capabilities. Only by characterizing each system can a true quantitative value be given to the errors present in the system. The next two sections review work that has been done on sensor characterizations and examines work that involves sensor error modeling.

2.2.1 Characterizations of Range Imaging Devices

Kweon et al. [11] published one of the first characterizations of the Perceptron AM laser range scanners. They address the issues of geometrical properties and nominal operating qualities of the scanner. They ascertain many of the sensor characteristics by observing images both spatially and temporally. Some of the effects they note are internal reflections, shadows, mixed pixels, and range drift. A statistical analysis determines the precision of pixel position and range measurement. The analysis associated with range measurement includes the effects of ambient light, surface material, incidence angle, and temperature.

In their discussion on the precision of the scanner, they conclude there is both a short term drift in range measurements of about $\pm$ 15cm and a long term drift associated with ambient temperature. Also, the standard deviation of range measurements for various surface materials is about 10cm except for materials close to the color black. For black colored objects, the standard deviation increases as the object's distance from the scanner increases. They discuss the accuracy of the scanner in terms of the RMS error. The RMS error varied from 0.08m to 0.56m for different surface materials. They also note that it is difficult to discern any trends in the RMS error because the sensor noise of 10-15cm dominates. Overall, they find the performance of the scanner does not compare favorably with the advertised performance.

Hoffman et al. [12] published an updated report characterizing the Perceptron LASAR 5000. Once again, their analysis includes matte surfaces with varying colors, angle of incidence, measurement drift, image stability, and metal targets. They conclude that reliable range measurements within 15mm can be obtained for a variety of matte materials. They give a formula that represents a good model of the sensor. Also for matte targets, range measurements are independent of incidence angle up to about 40 degrees. The accuracy of range measurements of metal targets is less than that for matte materials, but the precision of the measurements is comparable.

Davidson [13] performs a similar study on the Perceptron LASAR^{TM} 3D camera system with the goal of assessing the needed specifications for a 3D camera system required in the Light Duty Utility Arm project. Davidson notes several operating problems and shows a few limitations. To test the system, he builds several targets to exemplify possible problem areas. The targets include steps, "rubble beds", and PVC pipes of varying diameters. Davidson determines that errors in Cartesian range measurements are caused by the geometry of the spinning mirror along with the nodding mirrors. Also, he finds repeatability to be difficult due to the mirrors. The lack of repeatability causes blurring among multiple images of the same scene. Davidson defines a system's range as the standoff range plus the ambiguity interval. The standoff range is the shortest distance for valid range measurements, and the ambiguity range is where valid range measurements are taken. When the distance to an object exceeds the ambiguity range, the second ambiguity interval starts at the standoff range from the previous ambiguity interval. This standoff range, therefore, defines an area where no valid range data is acquired. System specifications of the Perceptron LASAR^{TM} 3D camera define the absolute range as starting from the standoff range and extending 10m beyond. Experimental results show the standoff range and the ambiguity interval combined are about 10m.

Pito [14] examines the Perceptron AM laser range scanner in a controlled environment for the purpose of acquiring highly accurate range maps for the application of automated CAD model acquisition. Pito derives an accurate model of the system and implements a calibration technique. He defines *micro-scale spatial range noise* as noise attributed by the local environment including the scene being ranged. He also defines *macro-scale spatial range noise* as noise due to complex interactions between the subsystems which measure phase (range) and intensity and problems in the electronics which cause range values to vary with intensity. He examines these issues along with mixed pixel spatial range noise, temporal spatial noise, angular spatial resolution, row misalignment, and banding. Due to the characteristics established by these results, he determines the Perceptron P5000 is unusable for his purpose. Pito states that the P5000 was not designed for this type of application, but remains hopeful that a customized version of the scanner will provide the needed accuracy.

Barry et al. [15] compare remote metrology techniques. They concentrate on the achievable accuracies, advantages, and disadvantages of ranging systems such as acoustical, structured light, synchronized scanners, fringe projection, time-of-flight laser radars, AM laser radar, and FM laser radar. They conduct a more in-depth study on the Coleman

FM imaging laser radar in which they resolve the sensor's sensitivity to materials, angle of incidence, range, and ability to image complex structures. The outcome of the experiment shows the Coleman system is more accurate than any of the other range scanning systems. Typical range measurements have a standard deviation of $\pm$ 0.5mm at 15m. The only disadvantage they give for the presently available Coleman scanner is the amount of time it takes to acquire an image. The system requires a significant amount of time to take data for two reasons. First, the mechanical scan method employed by the system is time consuming. Second, the use of multiple local oscillators to extend the coherence length of the laser diode further reduces the speed. The scanner must switch between oscillators to focus on different distances. Also, the cost of multiple oscillators makes the laser relatively expensive.

Hashemi et al. [16] discuss sources of error in a time-of-flight laser rangefinder. They present an equation for the standard deviation of statistical errors generated by quantization in the digital signal processing of the phase measurements which correspond to range. Also, they show how crosstalk and stray light give rise to errors that are cyclic with target range and explain possible techniques to reduce them. They illustrate the dependence of the photodiode's propagation delay upon the intensity and placement of the light spot incident upon its surface and provide a method for minimizing that effect. Other characterizations of various types of range imaging devices can be found in [17, 18, 19, 20].

2.2.2 Error Modeling of Range Imaging Devices

Sensors are essential to autonomous applications and the precision of the sensors can decide the accuracy of the robot motion, positioning, and object recognition. Often sensors are employed in applications that require accuracies that push the sensor to its limits. To be able to utilize a sensor to its fullest potential without having to make mechanical modifications, error modeling is needed to provide algorithms that are able to estimate errors in the sensor. At this point, it is necessary to define *error model*. The term error model applies to fully developed sensors that are calibrated (i.e. off the shelf systems). Ideally there should be no inaccuracies or imprecision.

In the real world, sensors still exhibit errors and they can be divided into two classes. The first class is systematic errors and the second class is random errors. Systematic errors are biases or other contingencies that are repeatable and can be corrected. Random errors are statistical and not repeatable, but they can be modeled through some type of statistical function. Therefore, a *correction model* is an algorithm or correction factor that represents the systematic errors in a sensor. An *error model* is a model of the *random* errors that remain after the correction model is applied. This section will give a short description of a correction model and an error model that have been developed for continuous-wave laser ranging systems and brief overviews of other error models.

Chen and Ni [21] describe a method for correcting erroneous range data in a Light Intensity Detection And Ranging (LIDAR) system. After developing the theory behind the scanners coordinate system, they explain a procedure to estimate the errors by using the intensity image generated by the scanner. They use a plane with five dark circles located in the field of view of the system. The centers of the targets and the distance between them are known. Thus, the real position and orientation of the target plane can be determined by minimizing the error between the estimated distances and the known distances. The formula for calculating the distance from the scanned point on the target plane to the LIDAR focal point is

$$R_c(r_i, c_j) = \sqrt{(x(r_i, c_j))^2 + (y(r_i, c_j))^2 + (z(r_i, c_j))^2}. \tag{2.6}$$

They obtain error in the range images by comparing the calculated distance to the measured distance:

$$e(r_i, c_j) = R_c(r_i, c_j) - R_m(r_i, c_j). \tag{2.7}$$

They use a polynomial regression to model the range image errors as a function of both range and intensity images, as follows:

$$e(r_i, c_j) = \sum_{k=0}^{p} \sum_{l=0}^{q} b_{kl}(R_m(r_i, c_j))^k (I_m(r_i, c_j))^l, \tag{2.8}$$

where the p and q are the order of the polynomial; b_{kl}'s are the parameters of the polynomial estimated by a least squares routine. This polynomial obtains a corrected range image by adding $e(r_i, c_j)$ to $R_m(r_i, c_j)$.

Hebert and Krotkov [9] derive an error model for AM continuous wave laser rangefinders. The model stems from the premise that the time-average radiant flux reaching the photodetector determines the quality of the range measurement. The flux is determined by

$$\overline{F}_P = k_1 \frac{\rho \cos \alpha}{r^2}, \tag{2.9}$$

where r is the range, α is the angle between the surface normal and the direction of the beam, ρ is the reflectance of the surface, and k_1 is a function of transmitted radiant flux, the capture area of the receiver, and filter bandwidths. Assuming that the output power of the photodetector is proportional to $\overline{F}_P$, the output signal is proportional to $\frac{\rho \cos \alpha}{r^2}$. Photon noise is the dominant source of inaccuracies and the equation for the signal-to-noise ratio is

$$SNR = k_2 (\frac{\rho \cos \alpha}{r^2})^{\frac{1}{2}}, \tag{2.10}$$

where k_2 is a scalar that depends on parameters of the sensor. Assuming a modulation of 100 percent, the effect of photon noise on the measured range value can be estimated by the standard deviation equation

$$\sigma_r \approx \frac{r_a}{\sqrt{2}\pi SNR}, \tag{2.11}$$

where r_a is the ambiguity interval. Combining (2.10) and (2.11) yields

$$\sigma_r = (\frac{r_a}{\sqrt{2}\pi k_2})(\frac{r^2}{\rho \cos \alpha})^{\frac{1}{2}}, \tag{2.12}$$

where the first term depends only on the physical, optical, and electronic characteristics of the sensor, and the second term depends only on the observed scene.

Adams et al. [10] develop a physical model of a continuous-wave light detection and ranging sensor in order to produce reliable range estimates and quantify the certainty in each range data point.

The literature contains a variety of other sensor models. Bajcsy et al. [22] present qualitative models for the errors and mistakes introduced in different stereo ranging systems. Matthies et al. [23] review existing models of the quality of range data from stereo vision and continuous-wave LADAR. They then use these models to derive a new model for the quality of a simple obstacle detection algorithm and test them with range data from stereo image pairs. Tamura et al. [24] correct range measurements of a structured light system by modeling the systematic errors based on the geometry of the scanning system. General models of sensors or the information they provide are given by Durrant-Whyte [25], Kanazawa et al. [26], and Abidi et al. [27].

CHAPTER 3

System Design

The goal of our project is to develop a system that is capable of obtaining high accuracy images with a time-of-flight laser rangefinder in a reasonable amount of time. This chapter describes the laser chosen for our project in terms of operational theory and interface capabilities. This chapter also describes our technique for moving the laser beam in order to create one-dimensional and two-and-half dimensional scans. It concludes with an overview of our simulation of the scanning system.

3.1 Characteristics of the Laser Rangefinder

The AccuRange 3000 Infrared Laser Rangefinder developed by Acuity Research, Inc. is the laser used in our system and error characterization. Figure 3.1 shows a picture of the AccuRange. The AccuRange has a wavelength of 780nm with an optical output power of 20 milliwatts.

Figure 3.1: *The AccuRange 3000 is a self-contained laser-diode-based distance measurement sensor. Power and signal cables connect to the back face of the sensor. The laser and collection optics are concentrically mounted behind the front face, with a 2.5 inch diameter collection area.*

The AccuRange projects a collimated beam of infrared laser light from the center of the front face. When the beam strikes an object, the sensor collects a fraction of the light scattered from the surface. The collection aperture consists of the area of the front face of the sensor surrounding the laser diode. The face focuses the returning light onto a photodetector. The laser beam (and the return signal) is amplitude modulated, and the sensor electronics use the outgoing and return signals to produce an electrical output signal with a period of oscillation proportional to the range[28].

Thus, the laser emits a beam of light carrying a square-wave pulse train of a predetermined length. The laser stays on until the photodetector detects the reflected light. The laser then shuts off and turns on again when the detector has received a percentage of the pulse train where this process is repeated. The laser turing on and off produces a frequency that is related to distance. The period of the signal is ~20ns at zero range and 280ns at 20m. Figure 3.2 shows the type of signal that the AccuRange uses along with when the laser turns on and off. The exact nature of the signal processing performed by the sensor electronics is proprietary pending the outcome of a patent application, but the method is purported to be similar to conventional phase comparison measurement techniques. The laser is modulated with a duty cycle of 50%, but the modulation waveform in not sinusoidal, and the electronics are substantially different from heterodyne phase-detection systems.

The AccuRange is connected to a computer by a SCSI interface. The interface sampling rate is variable from a maximum rate of 312,500 samples per second down to one sample approximately every 215 seconds. The different sampling rates are achieved by dividing the maximum rate by 2^N. In effect, the sampling rate defines a window of time that the laser allows for the system to achieve its beat frequency f_b. The resolution of the samples is proportional to the length of the pulse train emitted by the laser. The main limitation on resolution arises from the fact that the timing clock on the interface board runs at

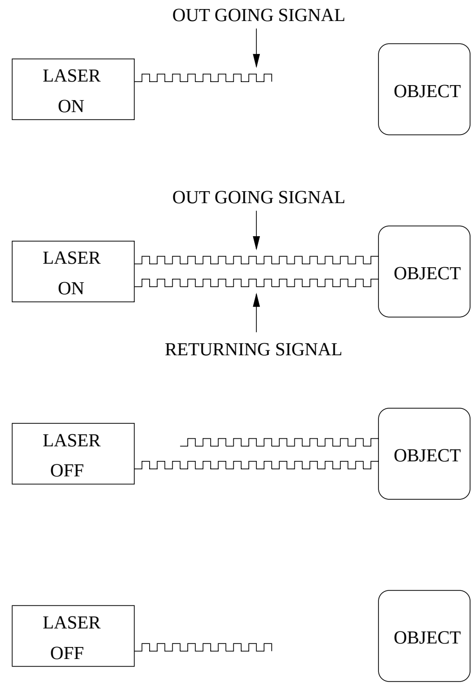

Figure 3.2: *A representation of how the AccuRange turns the laser on and off which produces a frequency that is related to range.*

80MHz, and as the sampling rate is increased, the resolution must be reduced to allow a complete sample to be taken in the sampling interval. With the interface board, the time necessary to take a sample depends on the range being measured. In practical terms, this limits the resolution to 0.4mm at 9760 samples per second for ranges < 2m, and 0.8mm for ranges up to 5m.

The board's SCSI interface is a standard 8-bit SCSI bus and uses asynchronous SCSI protocol to transfer data. The maximum transfer rate for the board is approximately 3 Megabytes per second, depending on the capabilities of the host computer. The board includes a 16 Kilobyte buffer for incoming data to accommodate SCSI latency.

3.2 Adding Degrees of Freedom

After selecting the type of laser rangefinder to be used, a major issue that needs to be addressed is how to move the laser beam around the designated area. Rotational mirrors provide a solution to this problem. They offer the advantage of moving the laser beam around the scene very quickly. Acuity offers the option of assembling the AccuRange with a 45 degree rotational mirror for the creation of a 1-D scan line. Figure 3.3 illustrates this arrangement.

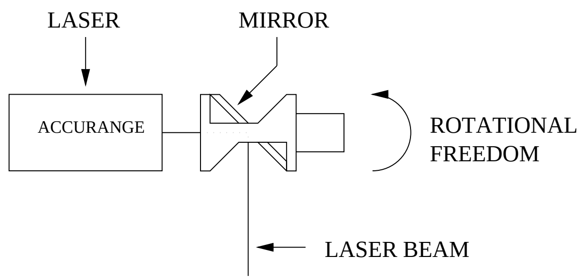

Figure 3.3: *Schematic of the AccuRange with the 45° rotational mirror which can be a one dimensional profiler.*

Although adding the rotational mirror solves our problem of moving the laser beam around in our designated area, it introduces a new problem. In many of our 1-D scans, spikes appear at the edges of objects. Part *(a)* of Figure 3.4 is a typical grayscale range image (darker is closer). Notice the white and dark areas at the edges of all objects. Part

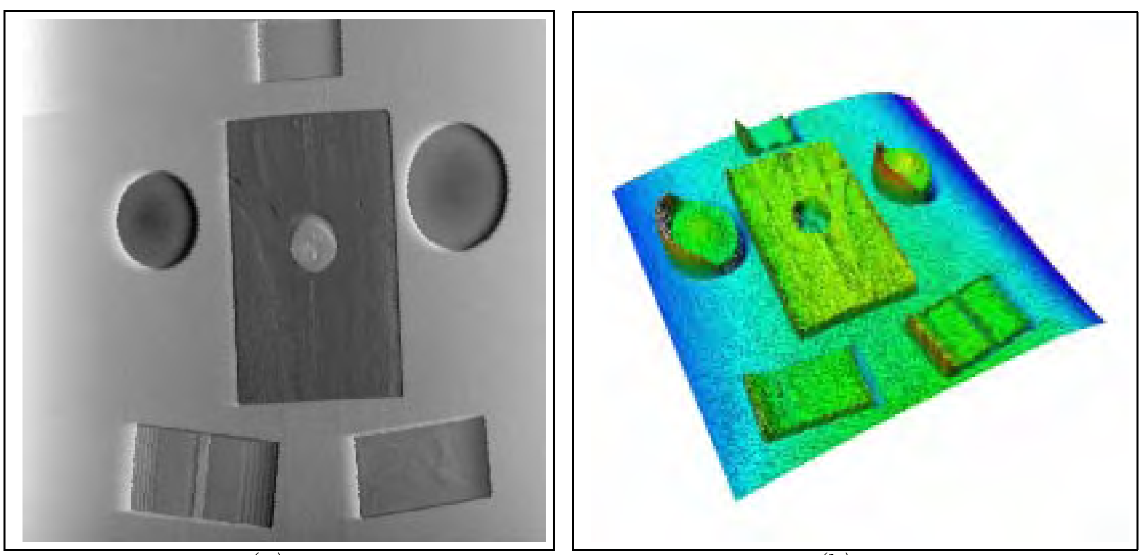

(a) *(b)*

Figure 3.4: *(a) Shows a typical color-coded grayscale range image. Notice the areas around each object. (b) Shows a 3-D representation of the range data. The spikes that surround each object are easily seen in this format.*

(b) shows a 3-D representation of the range data. Spikes are prevalent on all objects. Also, spikes are in the negative direction on the leading edge of objects and in the positive direction on the trailing edge of objects.

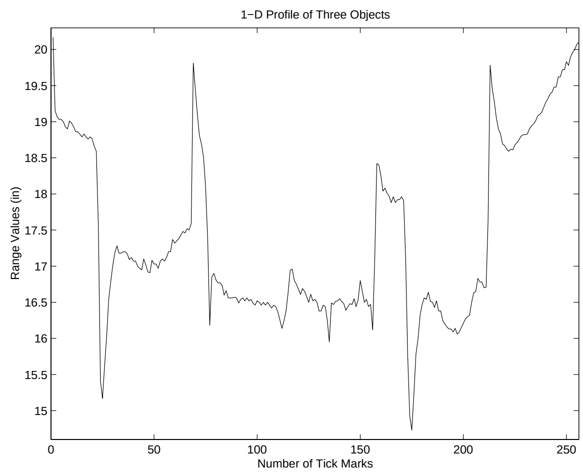

Figure 3.5: *This is a profile of a line taken from the image of the blocks. The line appears about one third the way down the image where the two round objects and the bigger middle object are located.*

Figure 3.5 shows a profile of a line out of the same block image. The spikes are large with respect to the size of the objects. Also, the spikes appear to have an exponential decay associated with them. We think this is due to some lag in the sensor electronics not being able to handle the quick change in distance. [1] These spikes are detrimental to our goal of a high accuracy scanning system.

To overcome the problem encountered with the mirror, we constructed a 3-D positioning system from LinTech linear positioning tables. Three, twelve inch ball screw tables are mounted in such a way as to give access to translational movement in the **X**, **Y**, and **Z** directions. Figure 3.6 shows this arrangement.

The positioning tables are capable of achieving a bi-directional repeatability of $+0.0002$ inches to -0.0082 inches with a position accuracy of < 0.0002 inch/inch and have a

[1] We sent the laser back to Acuity and had the electronics modified to increase the detector's sensing speed. After testing the system again, the same spikes appeared with less magnitude.

Figure 3.6: *Orientation of three linear positioning tables to provide access to the translational movement in the* **X**, **Y**, *and* **Z** *directions for the creation of range images using the AccuRange 3000 as a point laser.*

dynamic horizontal load capacity of 1550 lbs. Each table is driven by a Compumotor 2-phase hybrid permanent magnet motor. Figure 3.7 shows some common performance specifications for the motors. Each motor is operated by a PDS drive which connects into an AT-6400 indexer. The indexer is connected by SCSI interface to a PC, from which the system is programmed.

Performance	*Value*
Stepping Accuracy	± steps from preset total
Velocity Accuracy	± 0.02% of max rate above 1 rps
Velocity Repeatability	± 0.02% of max rate
Motor Resolution	25,000
Position Range	± 0 - 99,999,999 steps
Velocity Range	0.00001 to 50.0 rps 0.00001 to 35.0 rps (50,800 steps/rev) 0.00001 to 36.0 rps (50,000 steps/rev)
Acceleration Range	0.01 to 9999.99 rps^2

Figure 3.7: *Common specifications for the 2-phase hybrid permanent magnet stepper motor which drives the linear positioning tables.*

Figure 3.8 diagrams how the overall system is configured. The three linear stages overlook the scanning area while the connected laser points directly down into the area.

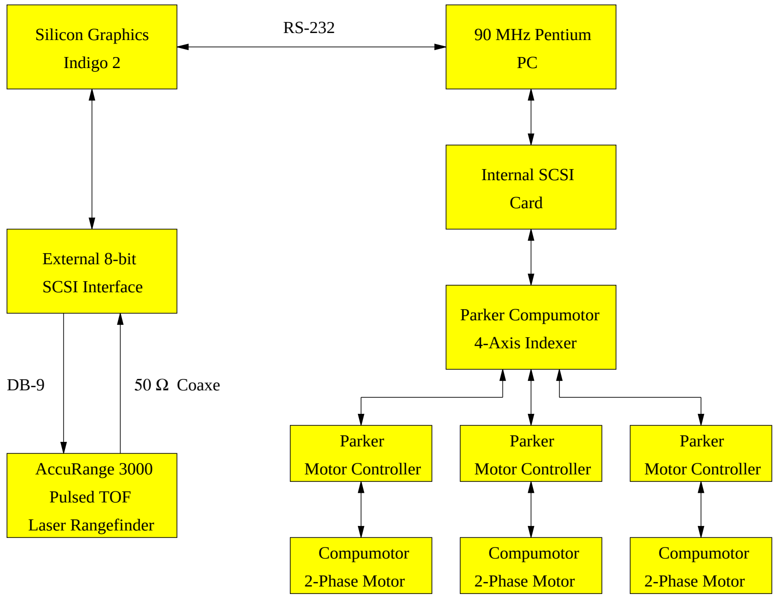

Figure 3.8: *Hardware diagram for our scanning system. Control of the laser is dedicated to the Silicon Graphics. Likewise, the linear stage positioning tables are governed by the PC. A reliable in-house serial communication library handles the information transfer between computers.*

3.3 Use of the Rotating Mirror

Although the results from the previous section illustrate the loss of accuracy incurred while using the AccuRange in conjunction with the rotating mirror, we have developed an interesting application for the mirror system where accuracy has a less significant role. This application for the mirror system would be used to take fast, broad scans of a desired region.

The new arrangement consists of mounting the AccuRange and the mirror to a rotational table forming a spherical scanning system. The perpendicular rotation of the table to the mirror creates the azimuth and elevation angles. Figure 3.9 shows the six inch rotational table used for this system.

The rotational table is connected similar to the linear stages described in the last section. The table is driven by a Compumotor 2-phase hybrid permenant magnet motor which is connected to a PDS drive. The PDS drive connects to the AT-6400 indexer which

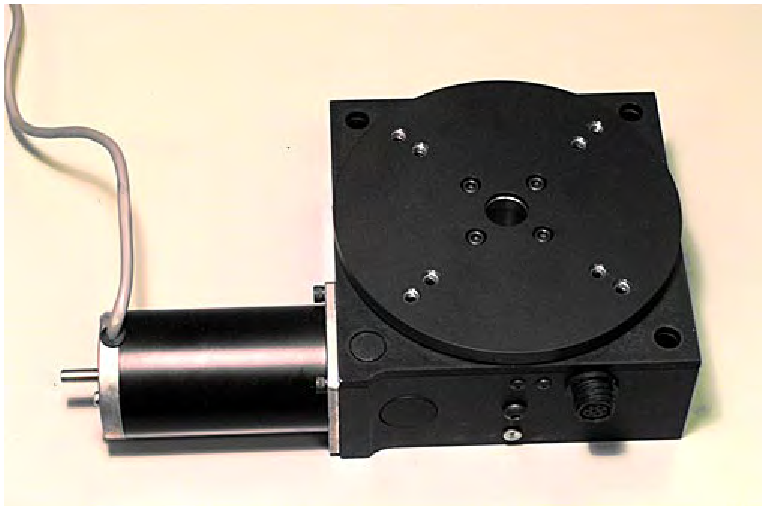

Figure 3.9: *LinTech's six inch rotational table which is capable of providing the constant rotation for our spherical scanning system.*

Performance		*NEMA 23 Motor Mount Bracket & Coupling*	
Unidirectional Repeatability	0.2 arc-min	Dynamic Moment Load	15 ft-lbs
Backlash	0.5 arc-min	Worm Gear Efficiency	50%
Accuracy	3.0 arc-min	Max. Input Speed	1800 rpm
Runout (Wobble)	$\pm$ 0.003 in	Max. Input Torque	500 oz-in
Concentricity	$\pm$ 0.0001 in		
Breakaway Torque	16 oz-in		

Figure 3.10: *Common specifications for the LinTech rotary positioning table and motor mount bracket.*

is connected by SCSI interface to a PC. Figure 3.10 shows some common performance specifications for the rotational table.

A control program on the Silicon Graphics machine operates the laser while communicating serially with the PC to coordinate the movement of the rotational table with the acquisition of data. The software for this system is operational and all hardware aspects have been worked out. Construction of two mounting plates is the only phase to be completed. Once these plates are in place, timing of the rotational speed of the table with data acquisition speed of the mirror and laser will need to be studied.

3.4 Simulation Model

Simulation, in general, is a tool for experimenting with physical systems based on idealized knowledge of their expected behavior. Simulations help us to better understand our designs, and to test them in situations which would be either too costly or entirely impossible in the real world. Traditionally, simulations are used as open-ended tools, i.e. all the information about the models exists at the beginning of a run, and in response to a set of recognized commands the simulation runs its course until a termination criterion is achieved. The ability to synthesize sensory information introduces new possibilities for analyzing sensory data: the real sensory data can be compared to synthesized information, and the deviations between the two can be used to identify errors in the real sensory data[29].

With this in mind, we designed a simulation model of our 3-D scanning system using Telegrip simulation software for similar purposes. Figure 3.11 depicts the system from two different angles. Control of the model is made possible through execution of programs written in Graphical Simulation Language (GSL).

The system operates on the same premise as the real scanning system. It reads an input file to acquire all operating specifications to perform as desired. The variables needed to run the simulation are the number of samples per line, number of lines, distances for each of the steppers to move, overall location of the platform to which the steppers are mounted, and a height for the movable scanning surface.

The only difference that is present in the simulation is the functionality of the laser. As described in the previous section, a sampling rate and resolution is required to operate the laser. These options are unable to be programmed in GSL. As with many of the CAD

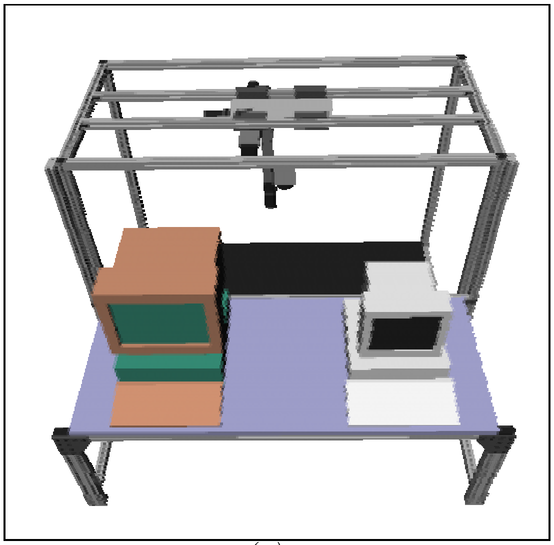

(a)

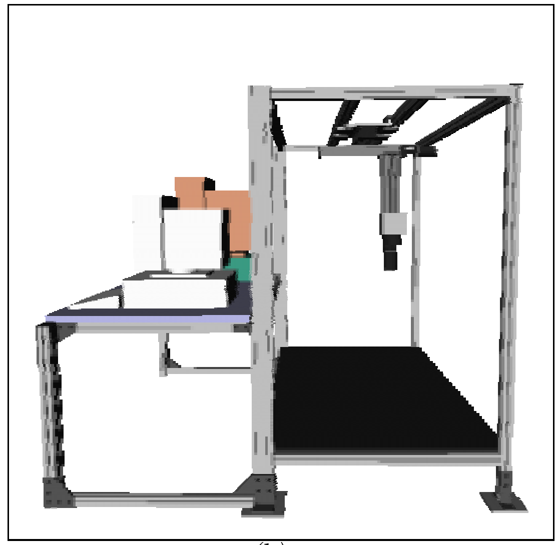

(b)

Figure 3.11: *(a) The frontview of the Telegrip simulation model which emulates our 3-D positioning laser scanning system which produces synthetic range images. (b) A sideview of the simulation model which shows the 3-D positioning possibilities of the linear tables.*

oriented simulation packages, Telegrip offers a function, RAY_CAST, that is capable of simulating the process of a laser. By assigning a reference vector and a directional vector, the simulation uses vector analysis to calculate the distance from this reference vector to the first surface it encounters along the directional vector. By moving the steppers in a serpentine manner, a range image with user-specified resolution can be created.

The laser also returns an intensity value which is a measure of the strength of the returned signal. This could be simulated in Telegrip by determining the color of the polygon used by the RAY_CAST function and the orientation of the polygon to determine a simulated signal strength. To determine the attenuated color of the polygon, one needs to evaluate the contribution of each light source in the workcell to the overall color of the polygon. In general, this can be quite difficult. As for the orientation of the polygon, it can be determined by using the return values from the RAY_CAST function. It would require a couple of matrix multiplications to resolve the returned surface normal into world coordinates. Due to the complex nature of these factors and time constraints, the

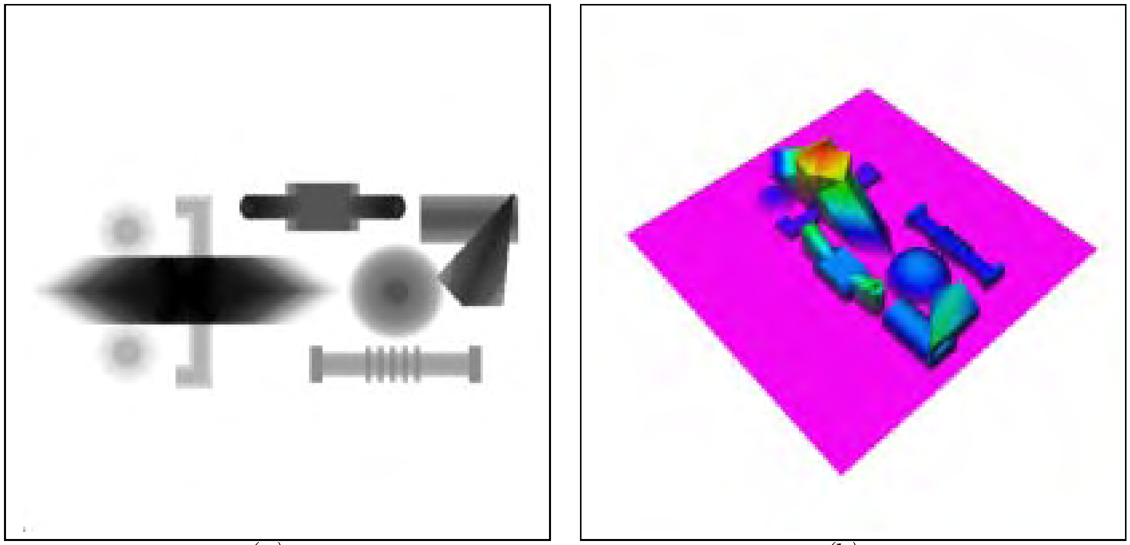

(a) (b)

Figure 3.12: *(a) A synthetic range image generated by our simulation scanning system that has been color coded according to range. The image demonstrates several types of phenomenon such as step edges, roof edges, and cylindrical properties. (b) An inverted 3-D representation of the same scene.*

implementation of this characteristic is not feasible.

An example of a synthetic range image created by the simulation model is shown in Figure 3.12. The image is 512 x 512 and is color coded according to the range values. One problem associated with using synthetic images for comparison with real images is registration. Developing a synthetic scene that portrays a real scene and scanning it in the same fashion as the real scanning system is by no means trivial. This type of comparison needs to be designed well and should only be made for strategic scenes that will demonstrate distinct aspects that lead to the characterization of errors.

Synthetic images are very beneficial for examining the properties of post-processing techniques. Without the ill effects of noise and random errors associated with range-imaging devices, synthetic range images allow for the processing technique to be analyzed for faults or failures. Also, this type of simulator is able to generate numerous scans of varying scenes.

CHAPTER 4

Error Characterization of the AccuRange 3000 as a Point Laser

With the background and system overview established from previous chapters, we begin our analysis of the AccuRange laser rangefinder from a point-laser perspective. The first sections describe some effects that pertain to the device electronics of the laser. These include temperature, pulsing the laser diode, and input parameters. The following sections detail errors that are present due to mixed pixels, target color, and incidence angle. The concluding sections develop a correction model and an error model based on experimental data.

4.1 Initialization

Common to all laser rangefinders is a fluctuation of range measurements due to temperature. Temperature can be broken down into two sources. The first is environmental temperature. Manufacturers give a span of temperatures that their laser should be operated in to avoid significant inaccuracies in range measurements. The AccuRange compensates for external temperature by scaling the raw range value accordingly. Because we are operating the laser in an indoor laboratory, we assume that fluctuations due to changes in environmental temperature should be limited. The second source of temperature fluctuation is device electronics. When the system initializes from a "cold" state, the system requires time for the temperature in the device electronics to stabilize. To test our laser, we took 500 measurements in one minute intervals for a two hour period at a distance of 19in. Figure 4.1 shows the average of the measurements for every minute for the two hour period.

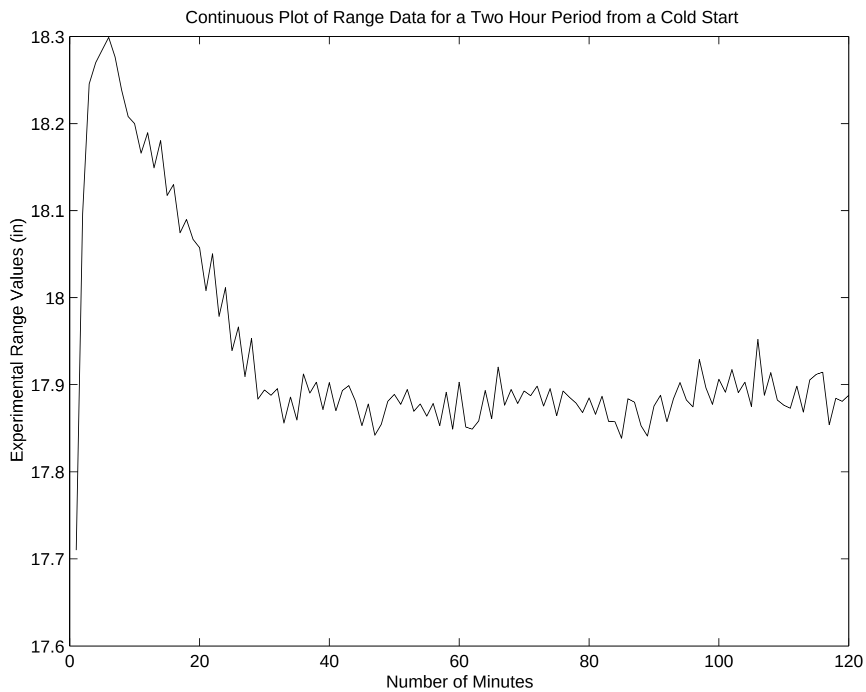

Figure 4.1: *A temporal plot of how temperature fluctuates in device electronics when the laser is started from a "cold" state. From this graph, we can estimate that a warm up time of about 25 minutes is required before temperature effects are minimized.*

The initial change in temperature of the device electronics causes an inflation in the range measurements. Several tests show that a warm up time of twenty-five to thirty-five minutes is necessary for the temperature to become stable.

Pulsing the diode creates another effect that needs to be taken into account. Turning on the diode reduces the accuracy of the first few range measurements of the sample set. This is due to changes in the diode itself as the laser is activated. We test the AccuRange by pointing the laser at a white target 20in away. The laser is turned on and 1000 range measurements are taken and the laser is then turned off. We repeat this method with nine different sampling rates. Figure 4.2 illustrates the results from our experiment. From the graphs, we see that the data reaches a plateau after this early enigma and no other irregularities appear. Figure 4.3 shows the same range measurements versus time. It is easy to see from the graphs that there is a finite amount of time when the diode is turned

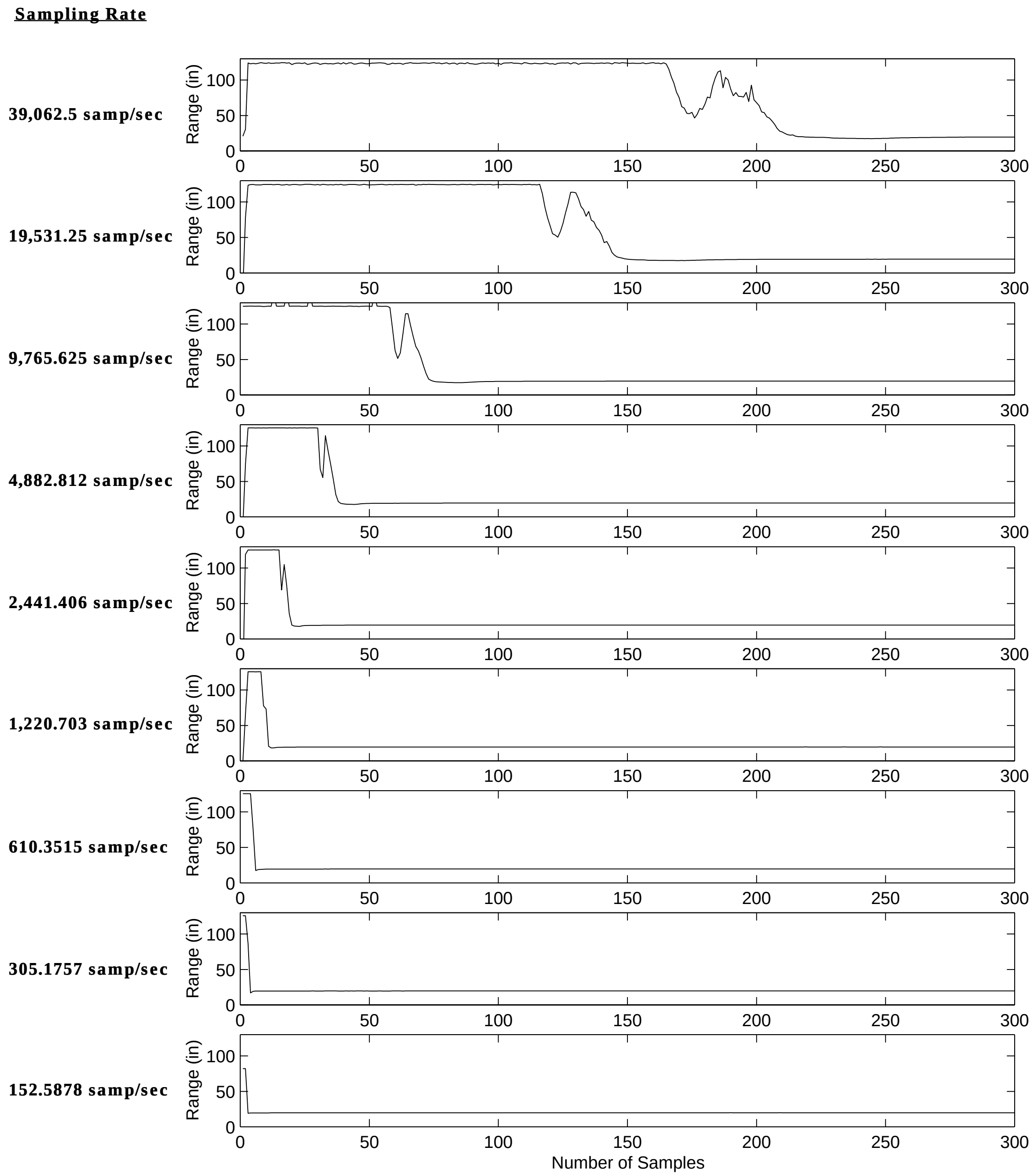

Figure 4.2: *The graphs illustrate how pulsing the laser diode at different sampling rates affect the accuracy of the range measurements at a distance of 20in.*

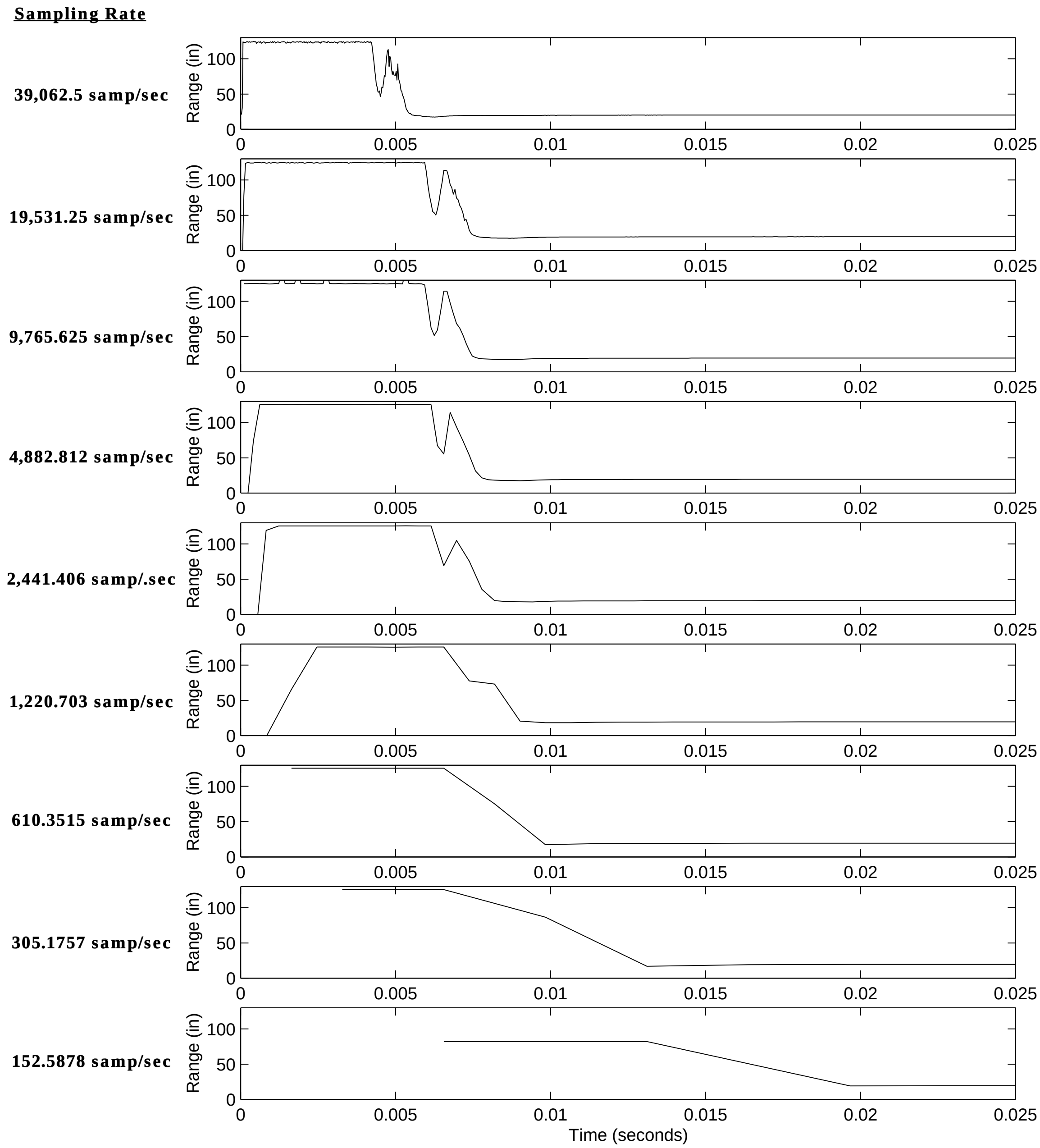

Figure 4.3: *The graphs illustrate that there is a finite amount of time when the laser diode is turned on that corrupted range data is produced.*

on that bad range measurements are produced. With the sampling rates that are available with the AccuRange, it is justifiable to use only the range measurements that are obtained after the signal is stable. All experiments from this point forward are conducted allowing for this transient behavior.

Also, the sampling rate, **M**, and resolution, **N**, can affect the range measurement. The time needed to take a sample depends on the range measured as well as the resolution selected. Acuity provides a chart that gives the maximum sampling rate for a complete sample at varying ranges. For our application, the distance is less than two meters. The chart gives a formula of $N = M + 3$ for this distance. Figure 4.4 gives a statistical analysis of the data from the discussion on pulsing the diode. The mean and variance of the measurements are calculated from 500 measurements of the stable part of the signal.

Resolution (mm/count)	*Sampling Rate (samples/sec)*	*Mean of Measurements (in)*	*Variance of Measurements (in)*	*R.M.S. Error (in)*
1.756	39,062.5	20.1585	0.00056	0.16027
0.8783	19,531.25	19.6935	0.00030	0.30703
0.4391	9,765.625	19.6488	0.00016	0.35143
0.2196	4,882.812	19.6358	0.00012	0.36435
0.1098	2,441.406	19.6714	0.00023	0.32897
0.05489	1,220.703	19.7187	0.00019	0.28163
0.02745	610.3515	19.8048	0.00021	0.19578
0.01372	305.1757	19.8576	0.00016	0.14501
0.006862	152.5878	19.8978	0.00014	0.10285

Figure 4.4: *The sampling rate and resolution has an impact on the accuracy of range measurements. The mean of the range measurements vary from 19.6358in to 20.1585in depending upon the sampling rate and resolution.*

The *mean* of the samples is calculated by

$$\mathcal{M} = \frac{\sum_{k=1}^{n} r_k}{n}, \tag{4.1}$$

where r_k is the experimental range measurement and n is the total number of measurements. An interesting observation about the different means is that all of them except one is less than the ground truth value of 20in. The ground truth value is the distance measured from the outside surface of the laser's filtering lens to the target surface.

The *variance* of the measurements is

$$\sigma^2 = \frac{\sum_{k=1}^{n}(\mathcal{M} - r_k)^2}{n}. \tag{4.2}$$

The variance is a measure of precision and for these point measurements the precision is high with all the values being less than one thousandth of an inch.

The *Root Mean Square* error of the measurements is

$$\mathcal{E}_{\text{rms}} = \sqrt{\frac{\sum_{k=1}^{n}(\mathcal{T} - r_k)^2}{n}}, \tag{4.3}$$

where $\mathcal{T}$ is the ground truth value. Notice how the accuracy of the measurements increases as the sampling rate is decreased with the exception of the first two sampling rates.

4.2 Fluctuations in Range Due to Environmental Temperature Changes

In the first section, we explained how effects from environmental temperature changes should be limited because of our controlled work space. After operating the laser for over a year, the situation appeared to be more complex. We have noticed fluctuations in range measurements as the environmental temperature drifts by only a few degrees. Figure 4.5 shows range measurements for four distances and various temperatures for a white matte surface.

It easy to see from the graphs that the same trend is prevalent at all distances. As the temperature rises, the range measurements become smaller compared to the ground truth distance. A change in temperature of only ten degrees results in a 0.25 to 0.60 inch change in the mean of the range measurements. The AccuRange software uses a lookup table that accounts for intensity and external temperature to produce calibrated range measurements. Our data shows that this process still has significant errors. [1]

[1] This effect was found at the end of our research process. During the error modeling and correction process, we noticed that images taken at different times of the year produced clearly different statistical characteristics. All of the work from this point on in this thesis does not factor in temperature.

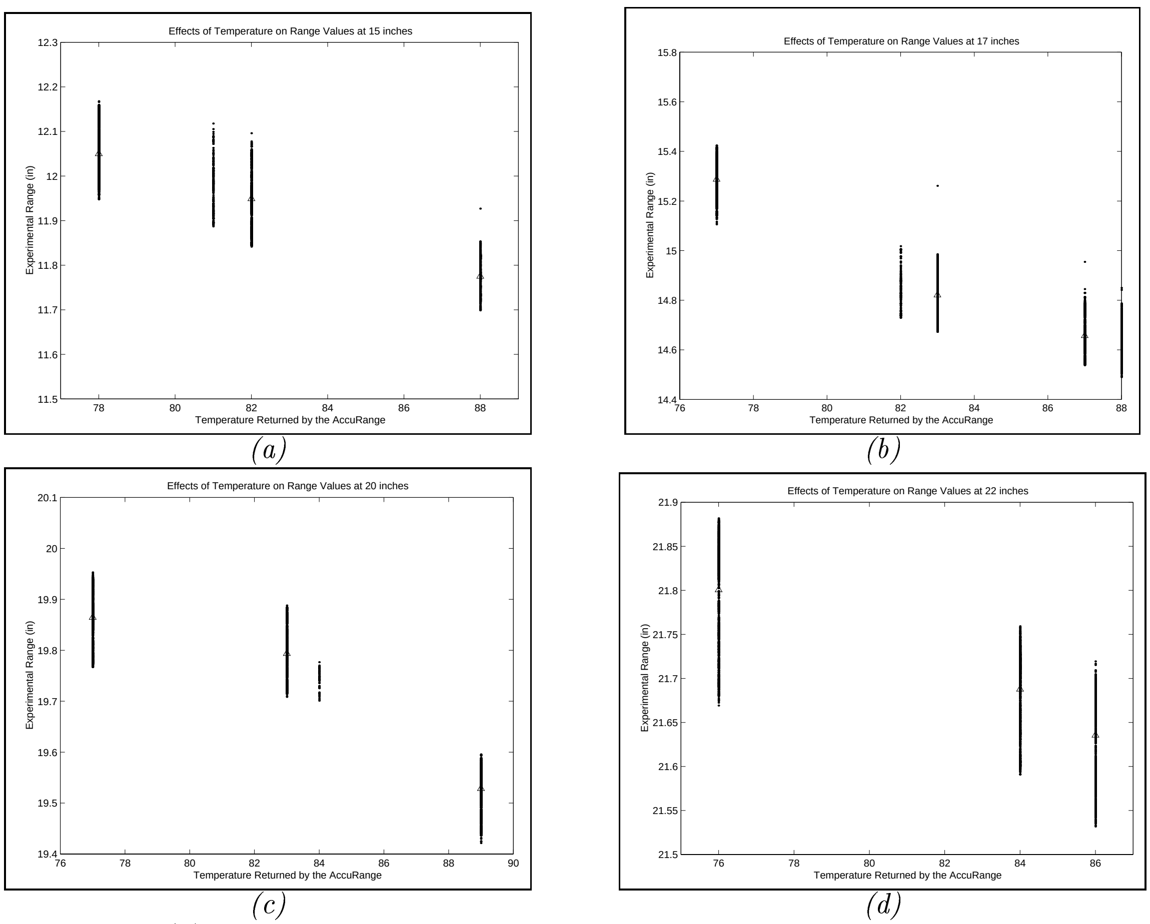

Figure 4.5: *(a) Range measurements versus temperature at a distance of 15 inches. The triangle represents the mean of the range measurements for that temperature. (b) At 17 inches. (c) At 20 inches. (d) At 22 inches.*

4.3 Mixed Pixels

As defined in Chapter 1, mixed pixels occur when the footprint of the laser beam falls on the edge between two surfaces which are located at different distances. Our laser has a footprint that is oval in shape and is approximately 3mm at its widest point. It is important to know what type of an effect mixed pixels have on range measurements in order to correct for them. To test how our laser handles this effect, we averaged 500 samples per measurement at 0.5mm increments as the beam moved across the edge of different sized blocks. Figure 4.6 shows the results of our experiment that used 1.25in and 3.375in wooden blocks.

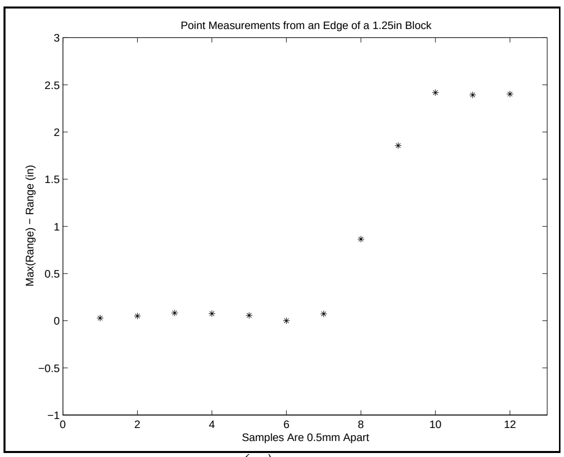

(a)

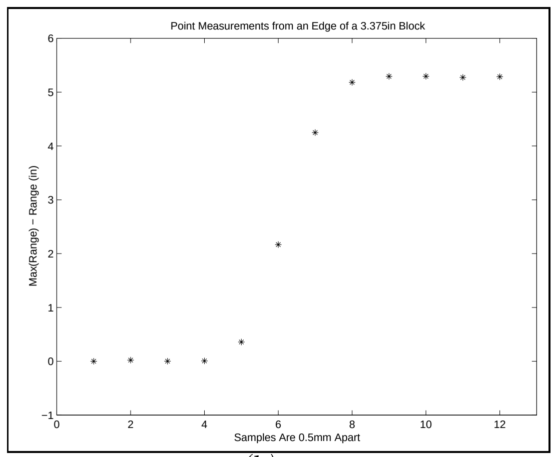

(b)

Figure 4.6: *(a) A plot of range measurements as the laser beam is moved in 0.5mm increments across a 1.25in block. The mixed pixel effect produces a range measurement that falls in between the farthest and closest surfaces. (b) The same test with a 3.375in block. The same effect is noted.*

The range measurements that occur while the beam is split between the two surfaces are in between the two surface distances. This is a minor degradation and no spikes are created. It will only cause the edge of objects to appear smoother than they really are. Recall when the laser was configured with the rotating mirror spikes in the negative and positive directions appeared on the edges of all objects.

4.4 Reflectance

Reflectance characteristics of surfaces play a significant role in the errors associated with range measurements. The reflectance of an object may add or subtract from the signal depending on the value of reflectance and the spectrum of light being projected onto the object. Usually, low values of reflectance corrupt the signal by absorbing some of the signal which slows down the pulse frequency of the laser. The range measurements are determined from this frequency and become inflated because the laser believes the object is farther away. High values of reflectance corrupt the signal by producing specular reflections which tend to saturate the photodetector. This saturation causes the pulse frequency of the laser to become erratic and can cause objects to appear closer than they really are. Depending upon the wavelength of the laser light, effects of these factors will vary.

The experimental setup to analyze these effects consists of measuring various reflectance values at different distances and comparing the results. For these tests, the laser beam is perpendicular to the target surface to minimize errors due to loss of signal. Six matte surfaces with increasing grayscale values are at ranges of 10, 15, 20, 25, and 30in.

Figure 4.7 shows a three-dimensional plot of the mean of the experimental range measurements versus the actual range for all grayscale values. From the plot, the relationship between reflectance and distance appears to be linear.

A linear regression shows that our observation that range is linear with respect to distance is correct. Figure 4.8 shows the linear regression line along with all the mean values at the intermittent distances. The equation for the line is

$$r = 0.9804\mathcal{T} - 0.6732, \tag{4.4}$$

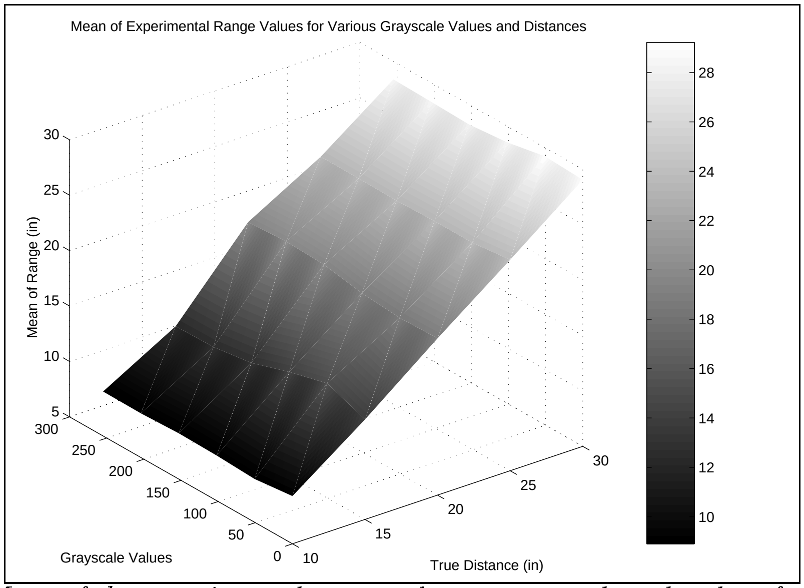

Figure 4.7: *Mean of the experimental range values vs. ground truth values for all grayscale values.*

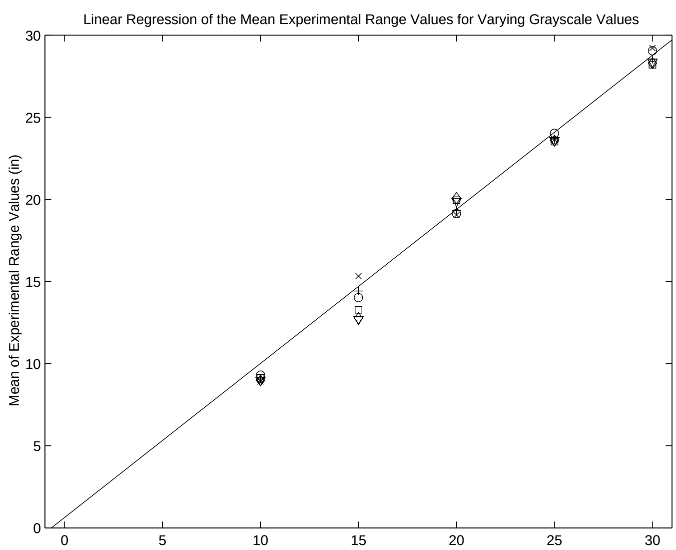

Figure 4.8: *A plot of the mean of the experimental range values versus the ground truth distance for all six grayscale values. The line represents a linear regression performed on the means.*

where r is the experimental range measurement and $\mathcal{T}$ is the ground truth distance.

This result substantiates our observation. Notice that there is an offset associated with the equation. As a whole, the experimental range measurements are less than the ground truth values and the term 0.6732 represents this offset in the equation.

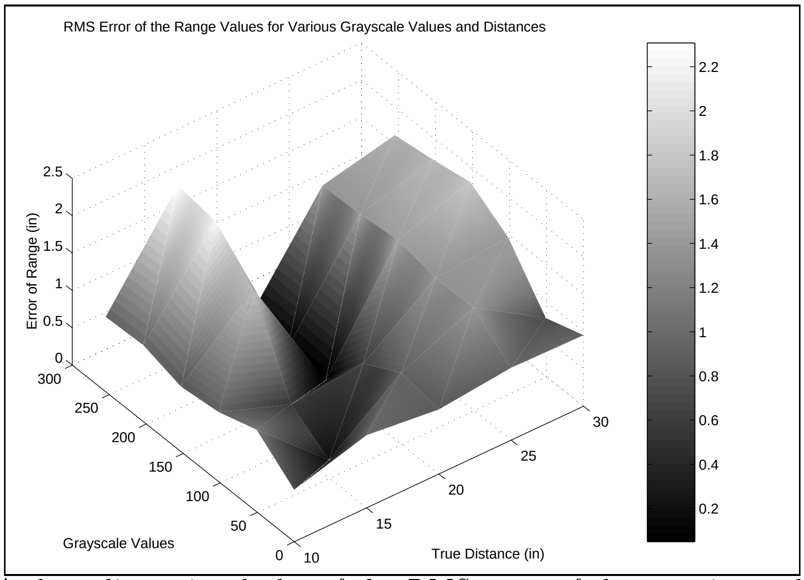

Figure 4.9: *A three-dimensional plot of the RMS error of the experimental range values for all grayscale values.*

Figure 4.9 shows the RMS error for our experimental range measurements. Our scanner functions the best at 20in. The RMS error of the range measurements is calculated by Equation 4.3. At 20in, the RMS errors for grayscale values between 102 and 255 have a mean of 0.2281in. The RMS error for all grayscale values is 1.0693in.

4.5 Angle of Incidence

Angle of incidence is another substantial contributor to the error present in laser range data. This is because laser rangefinders rely on the detection of reflected signals. If the signals are intersecting with a target at an angle, a portion of the signal will not be reflected back in the direction of the detector. The error increases with increasing angle of incidence.

The previous experiment indicates that our scanner provides the most accurate range measurements at 20in. For this reason, we chose to study the effects of angle of incidence at this distance for various grayscale values. Figure 4.10 shows the mean of the experimental range values for varying grayscale values at incremental angles of incidence.

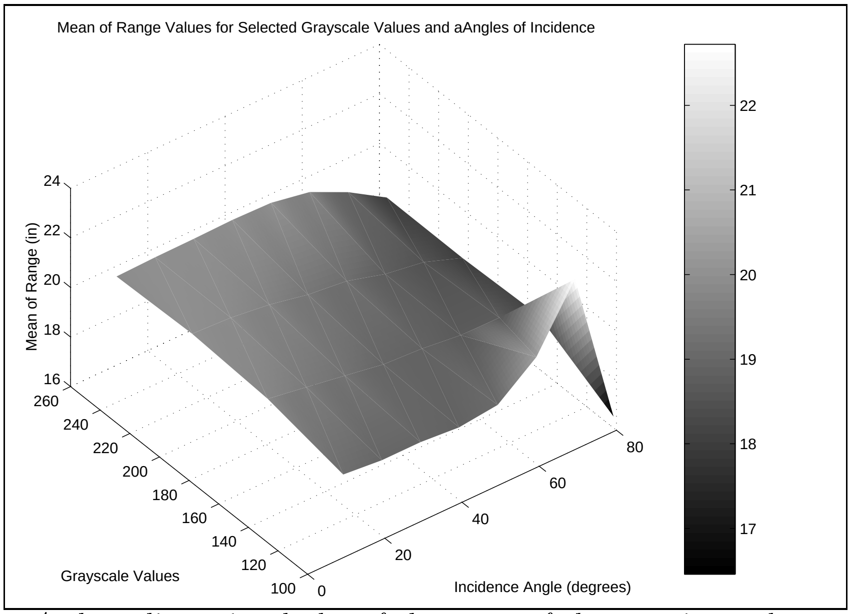

Figure 4.10: *A three-dimensional plot of the mean of the experimental range values for grayscale values* $\geq$ *102 at incremental angles of incidence.*

For grayscale values of 0 and 51, the experimental range measurements become very corrupted and extremely low mean values are achieved. For this reason, they are not included in Figure 4.10. The remaining grayscale values exhibit a somewhat linear error in the range measurements for angles less than 60 degrees. Our confidence level in the range measurements drops after 60 degrees because the plot shows an unpredictable nature to the range measurements pass this point.

Figures 4.11 and 4.12 show the RMS error in the mean of the experimental range measurements versus the incremental angles of incidence. Figure 4.11 illustrates the problems associated with black to near-black surface colors for this experiment. Figure 4.12 is a similar plot that excludes the range measurements for the grayscale values of 0 and 51.

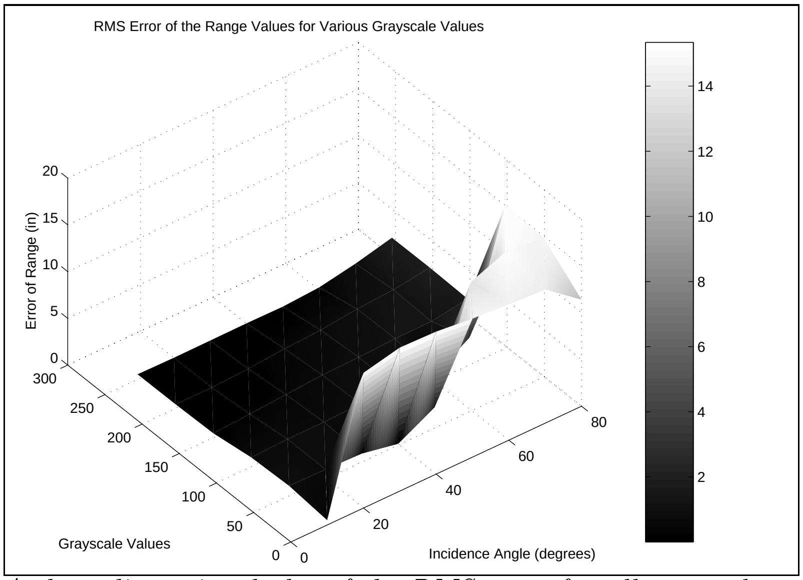

Figure 4.11: *A three-dimensional plot of the RMS error for all grayscale values at incremental angles of incidence.*

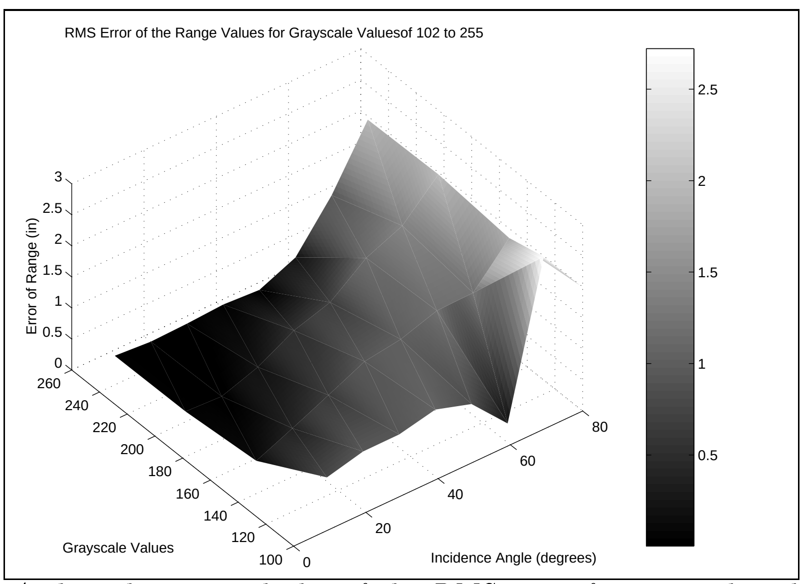

Figure 4.12: *A three-dimensional plot of the RMS error for grayscale values* $\geq$ *102 at incremental angles of incidence.*

All of the experiments have identified some type of noise attributed to some factor. Figure 4.13 gives a review of the results from the experiments and attempts to classify the errors according to cause, random or systematic and indicator the error present. We only use the information generated by the laser as our indicator. The range is the returned range by the laser rangefinder and the amplitude is the magnitude of the returned signal. The temperature reading is generated by a sensor that is part of the laser rangefinding system provided by Acuity.

Cause of Error	*Type of Error*	*Indicator of Error Expected Magnitude*
device electronics	random	amplitude
environment temp.	systematic	temperature
samp. rate/resol.	random, systematic	range, laser settings
mixed pixel	systematic	amplitude, range (derivatives)
reflectance prop.	random, systematic	amplitude, range
incidence angle	random, systematic	amplitude, range (derivatives)

Figure 4.13: *Classification of the errors determined from the previous experiments.*

4.6 Development of an Error Correction Model

The error sources identified in the previous section contain both systematic and random errors. Our goal is to correct for the systematic errors and reduce the magnitude of the random errors. By operating the laser after it has been allowed to warm-up and using the same sampling rate and resolution value for all of our tests, the effects of these two contributing factors should be limited. The mixed pixel effect should not be a major contributor either because of the smoothing effect that occurs with our laser. The angle of incidence degrades the range measurements for angles larger than fifty to sixty degrees. Because these sharp angles represent such a small number of the total number of data points in an image, their effect is not considered to be of great concern. This leaves reflectance properties of objects and varying measurement distances as the main contributors of systematic error. To correct for these factors, we need to develop a method for obtaining data which accounts for both of these factors and use the data to generate a correction model.

Our approach is to model the systematic errors by analyzing experimental range measurements. This is done by taking range measurements of various grayscale colored planes at various distances. Then we calculate the error of each range measurement by

$$\mathcal{C}_k = \mathcal{T}_k - r_k, \tag{4.5}$$

where $\mathcal{T}_k$ is the true distance and r_k is the range measurement. We define the error as our correction factor. Next, we plot the experimental range and experimental intensity vs. correction factor [30]. We then fit a surface to the plot which becomes our correction model for the sensor.

A polynomial fit derived from the single value decomposition (SVD) method is how we fit the surface to the correction data. In the case of an overdetermined system, SVD produces a solution that is the best approximation in the least-squares sense [31]. The matrix representation of our surface fit is given by

$$\mathbf{A} \cdot \mathbf{x} = \mathbf{b}, \tag{4.6}$$

where $\mathbf{A}$ is a matrix containing the polynomial we are fitting to the 3-D error plot, $\mathbf{x}$ is a matrix containing the variables we are solving for and $\mathbf{b}$ is a matrix containing the correction factors associated with range and intensity pairs used in the polynomial for $\mathbf{A}$. The elements of $\mathbf{A}$ are obtained from the minimized polynomial represented by

$$(1 + r_k + i_k)^n = \sum_j (\alpha_k)_j, \tag{4.7}$$

where $a_{k,j} = (\alpha_k)_j$, x_j is the coefficient associated with this term and r_k, i_k are the range and intensity for the k^{th} measurement.

There are several steps in the process to compute $\mathbf{x}$. The first step is to take the SVD of $(A^T A)$ which produces the three matrices $\mathbf{U}$, $\mathbf{S}$, and $\mathbf{V}$. The matrix $\mathbf{S}$ is diagonal with the same dimensions as $A^T A$ and has nonnegative diagonal elements in decreasing order. The matrices $\mathbf{U}$ and $\mathbf{V}$ are column-wise orthonormal such that

$$\mathbf{A^T} \cdot \mathbf{A} = \mathbf{U} \cdot \mathbf{S} \cdot \mathbf{V^T}. \tag{4.8}$$

The second step is to threshold and invert $\mathbf{S}$. The diagonal entries of the matrix are divided by the first entry and checked to determine if they are greater than 10^{-15}. If they are not, then the entry is replaced with a zero. This is to keep the magnitude of the entries from becoming unmanageable during the inversion process. Once $\mathbf{S}$ has been inverted, $\mathbf{x}$ is computed by

$$\mathbf{x} = \mathbf{V} \cdot \mathbf{S^{-1}} \cdot \mathbf{U^T} \cdot \mathbf{A^T} \cdot \mathbf{b}. \tag{4.9}$$

Figure 4.14 is a replica of the matte surface that we scan at distances of 15, 17, 20, and 22in to create our experimental data. The chart starts at a grayscale value of 0 for white and increments by 51 until a grayscale value of 255 for black is reached.

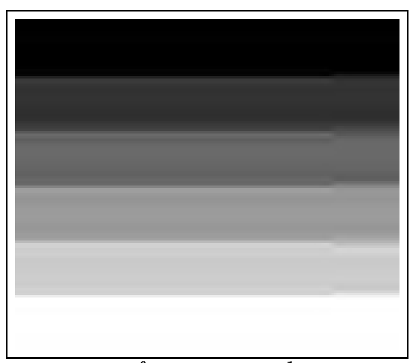

Figure 4.14: *A replica of the matte surface we used to scan to generate our experimental range data for our error correction model.*

Figure 4.15 shows a three dimensional plot of the experimental range and intensity data versus the correction factor for each range measurement in part (a) and a three dimensional plot of the surface that was generated by a fourth-order polynomial to the correction data in part (b).

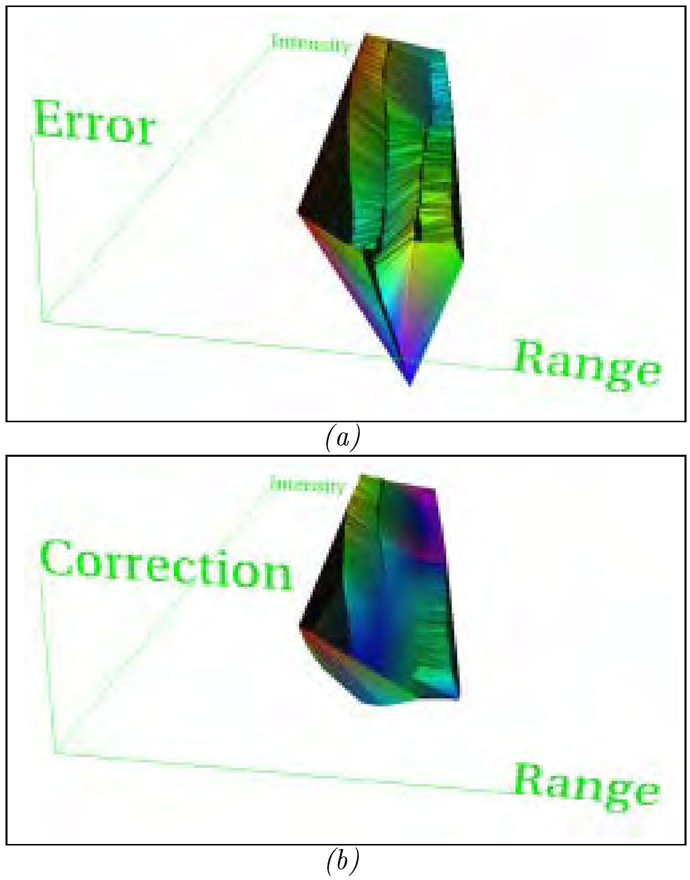

Figure 4.15: *(a) Plot of range and intensity vs. error for the matte surface measured a point at a time at distances of 15, 17, 20, and 22in. (b) Plot of range and intensity vs. correction factor generated by our method of surface fitting using a fourth-order polynomial to the error in part (a).*

Figure 4.16 shows how well our generated surface fits the correction data for the point-by-point method. The *mean error* of the points is calculated by

$$\mathcal{E}_m = \frac{\sum_{k=1}^{n} |\mathcal{C}_k - \mathcal{G}_k|}{n}, \tag{4.10}$$

where $\mathcal{C}_k$ is the correction factor and $\mathcal{G}_k$ is the correction factor generated by our polynomial fit.

Order of the Polynomial	*Mean Error of Fit (in)*	*RMS Error of Fit (in)*
Third	0.004882	0.346634
Fourth	0.016943	0.313503
Fifth	0.002392	0.132545
Sixth	0.001269	0.108443

Figure 4.16: *Shows a statistical analysis of how our generated surfaces fit our correction data for the point-by-point method.*

To test our correction model, we took a profile of the same matte surface at a distance of 19in. This is a value that is in between our test data set we used to create our correction model. Figure 4.17 shows the raw range measurements in part (a) and the corrected range measurements using the fourth-order polynomial fit in part (b). Figure 4.18 shows a summary of the results of several polynomial fits. The *bias* of the measurements is determined by

$$\mathcal{B} = \mathcal{T} - \mathcal{M}, \tag{4.11}$$

where $\mathcal{T}$ is the ground truth value and $\mathcal{M}$ is the mean of the measurements.

Notice how the higher-order polynomial fits produce corrected range values that are less accurate than the lower polynomial fits. This is because the higher order polynomials become unstable for points that are not a representative of the range of distances and intensities used to generate the surface.

Figure 4.19 shows a breakdown of the RMS error for the six grayscale colors present in our matte surface. The improvement after applying our correction algorithm is clearly

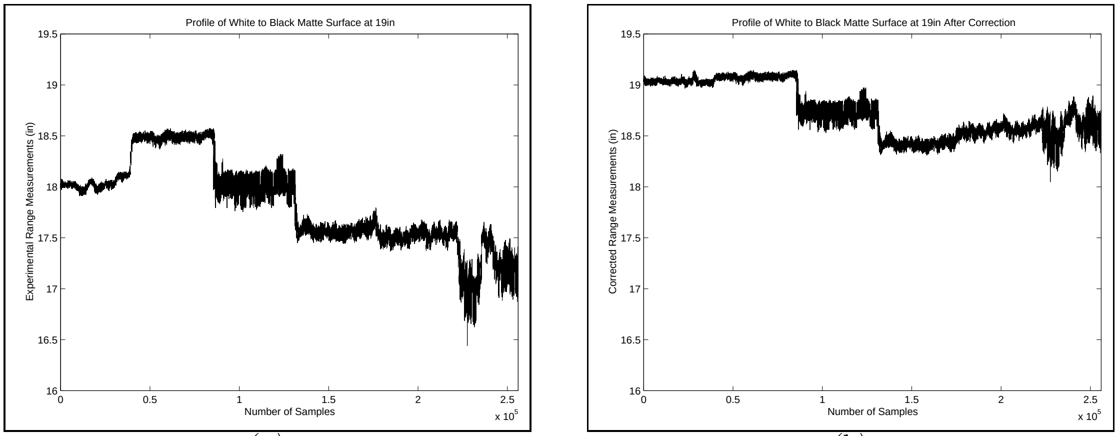

(a) (b)

Figure 4.17: *(a) A profile of the matte surface taken at 19in. (b) Corrected range measurements of the same profile using the fourth-order polynomial correction surface.*

Order of the Polynomial	*Bias of Data (in)*	*Variance of Data (in)*	*RMS Error of Data (in)*	*Improvement of Bias (%)*	*Improvement of RMS Er (%)*
Raw Data	1.16721	0.17745	1.24090	N/A	N/A
Third	0.25710	0.10289	0.41109	77.97	66.87
Fourth	0.25932	0.06376	0.36195	77.78	70.83
Fifth	0.63784	0.05426	0.67905	45.35	45.28
Sixth	0.63795	0.03587	0.66548	45.34	46.37

Figure 4.18: *Shows a statistical analysis between the raw data and the corrected data using our four different polynomial fits. From the data, the fourth-order polynomial produces the most accurate and precise correction data for the profile shown in the last figure.*

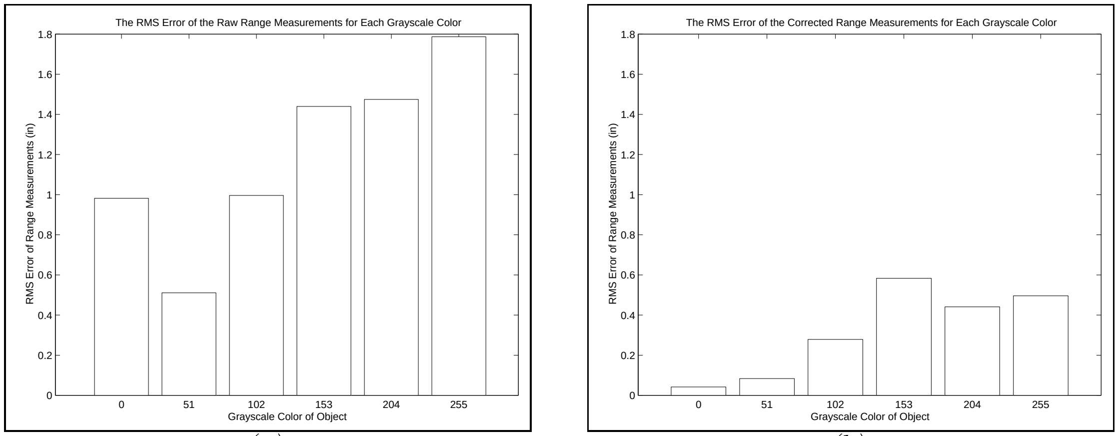

(a) (b)

Figure 4.19: *(a) A comparison of the RMS error of the raw range measurements taken with the point-by-point method for each grayscale color at a range of 19in. (b) A comparison of the RMS error of the corrected range measurements for each grayscale color at the same distance.*

evident from these graphs.

4.7 Alternative to Point-by-Point Method

We have developed an alternative to the point-by-point method described in the previous section due to the time required to take an image. This method operates line by line. It starts the laser and moves the beam while the laser is taking measurements. There are some important details regarding this method. Due to fluctuations in sampling rate and the mechanical movement of the laser, the number of samples taken by the laser per line is not constant. To correct this problem, we use a weighted average of the total samples per line. For example, with the adjustable sampling rate of the laser and the controllable speed of the positioning system we can take samples that overlap. This produces thousands of the range measurements per line. After determining the number of samples desired, we divide the total number of range measurements by the number of desired samples to produce the number of weighted range measurements to attribute to a sample.

After a few images, we noticed that when the beam is moving the laser produces a different range measurement than when it is still. This requires us to generate a new correction model for this method. The same image from the last section was scanned at 15, 17, 20, and 22in to produce our experimental data for our correction model. Figure 4.20 shows a plot of the experimental data in part *(a)* and the surface fit that was generated by a fifth-order polynomial in part *(b)*. Figure 4.21 shows how well our generated surfaces fit the correction data for the line-by-line method.

To test our correction model, we took an image of the same matte surface at a distance of 19in. This is a value that is in between our test data set we used to create our correction

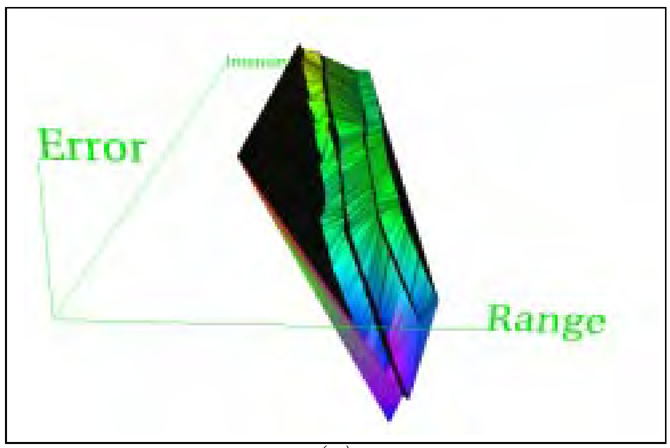

(a)

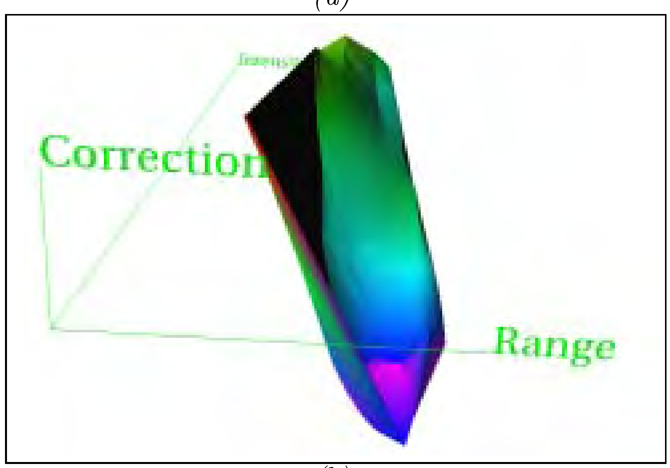

(b)

Figure 4.20: *(a) Plot of range and intensity vs. error for the matte surface measured a line at a time at distances of 15, 17, 20, and 22in. (b) Plot of range and intensity vs. correction factor generated by our method of surface fitting using a fifth-order polynomial.*

Order of the Polynomial	*Mean Error of Fit (in)*	*RMS Error of Fit (in)*
Fourth	0.29711	0.98336
Fifth	0.00104	0.19229
Sixth	0.00144	0.18819

Figure 4.21: *Shows a statistical analysis of how our generated surfaces fit our correction data for the line-by-line method.*

model. Figure 4.22 shows the raw range image in part (a) and the corrected range image using the fifth-order polynomial fit in part (b). Figure 4.23 shows the statistics of several polynomial fits. Notice that once again the higher-order polynomial fits produce a less accurate corrected range value. Figure 4.24 shows a summary of the statistics of the RMS error for the six grayscale colors present in our matte surface. As with the point-by-point method, a grayscale color of 255 produces the largest amount of error.

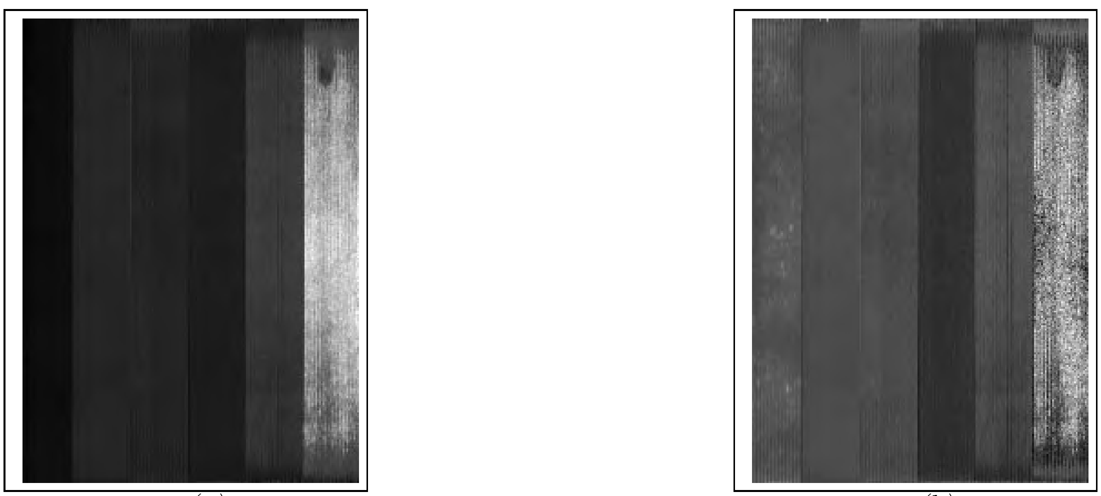

(a) *(b)*

Figure 4.22: *(a) A range image of the matte surface taken at 19in. (b) Corrected range image of the same surface using the fifth-order polynomial correction surface.*

To further test our correction model, we created a checkered board pattern matte surface of random grayscale values shown in Figure 4.25. Figure 4.26 shows the raw range image in part (a) and the corrected range image using the fifth-order polynomial fit in part (b).

Order of the Polynomial	*Bias of Data (in)*	*Variance of* Data (in)	*RMS Error of Data (in)*	*Improvement of Bias (%)*	*Improvement of RMS Er (%)*
Raw Data	0.1264	0.88461	0.94899	N/A	N/A
Fourth	0.0553	0.09607	0.31485	56.25	66.82
Fifth	0.0681	0.08919	0.30631	46.12	67.72
Sixth	0.4917	0.33859	0.76185	-289.00	19.71

Figure 4.23: *A statistical analysis between the raw data and three different polynomial fits to the correction data. From the data, the fifth-order polynomial produces the most accurate and precise correction data for the profile shown in the last figure.*

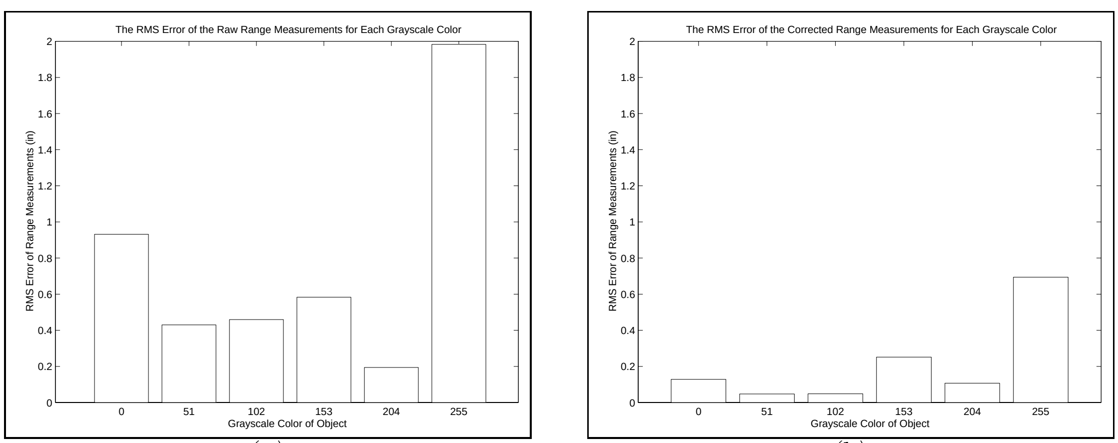

(a) *(b)*

Figure 4.24: *(a) A comparison of the RMS error of the raw range measurements taken with the line-by-line method for each grayscale color at a range of 19in. (b) A comparison of the RMS error of the corrected range measurements for each grayscale color at the same distance.*

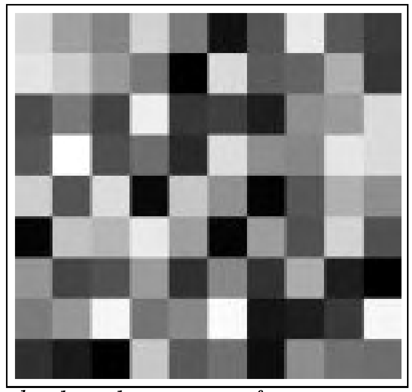

Figure 4.25: *A replica of the checkered matte surface we scanned to generate experimental range data to test our correction model.*

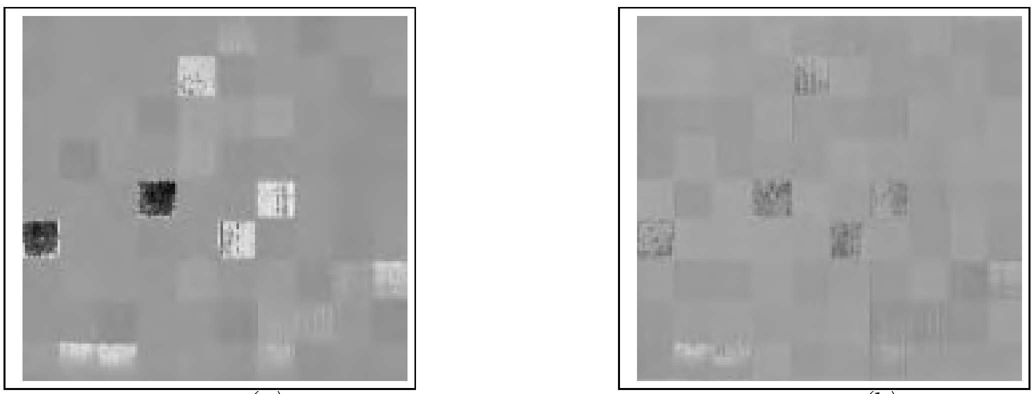

(a) *(b)*

Figure 4.26: *(a) A range image of the matte surface taken at 18in. (b) Corrected range image of the same surface using the fifth-order polynomial correction surface.*

Figure 4.27 shows the statistics of several polynomial fits. The bias, variance, and the RMS error of the raw range data is worse than for the previous stripe image. This is attributed to the changes of color. We have concluded that the device electronics for the AccuRange laser rangefinder cannot handle rapid changes in color or distance without errors becoming overly apparent in the system's results.

The spikes that are prevalent on the edges of objects when the laser beam is swept across a scene demonstrated the difficulties the system has with rapid changes in distance. Figure 4.28 shows the difficulties the system has with rapid changes of color. Part *(a)* shows a line scan of a black matte surface at 19in. The raw range values of this line vary

Order of the Polynomial	*Bias of Data (in)*	*Variance of Data (in)*	*RMS Error of Data (in)*	*Improvement of Bias (%)*	*Improvement of RMS Er (%)*
Raw Data	0.42263	1.88368	1.43607	N/A	N/A
Fourth	0.39736	1.73512	1.37587	5.97	4.19
Fifth	0.14863	0.31219	0.57817	64.83	59.74
Sixth	0.08793	5.39887	2.32521	79.19	-61.91

Figure 4.27: *Shows a statistical analysis between the raw data and three different polynomial fits to the correction data. From the data, the fifth-order polynomial produces the most accurate and precise correction data for the image shown in the last figure.*

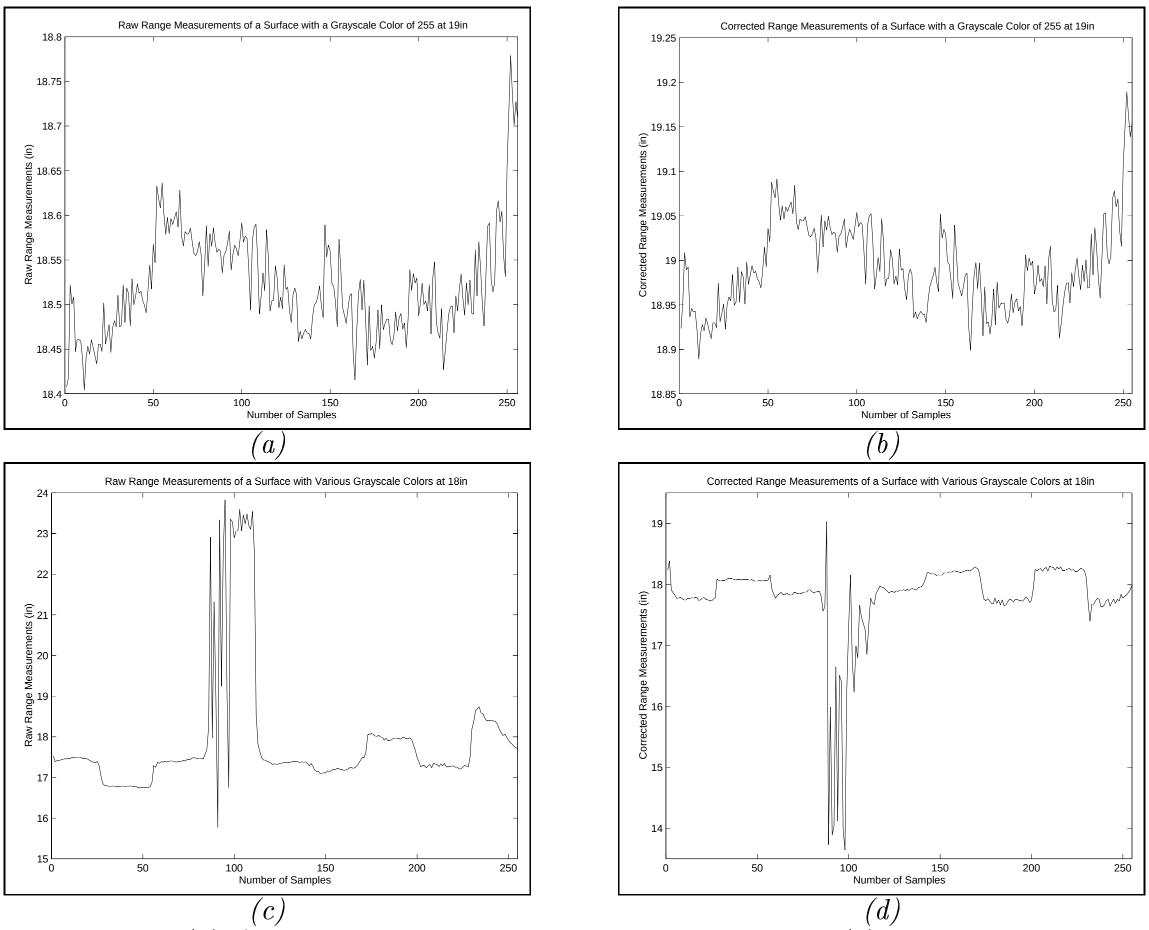

Figure 4.28: *(a) A line scan of a black matte surface at 19in. (b) The corrected range values for the line in the previous part. (c) A line scan of various grayscale colors at 18in with the color black producing range measurements with the most noise. (d) The corrected range values for the line in the previous part.*

from 18.41in to 18.78in. Part *(b)* shows the corrected range values of the line and they vary from 18.89in to 19.19in. Part *(c)* shows a line scan of a matte surface with various grayscale colors at 18in. For the color black in this line scan, the raw range values vary from 15.65in to 23.91in. Part *(d)* shows the corrected range values for the color black and they vary from 13.55 to 19.10in. The device electronics seem to not be able to handle the rapid change in color from mid-gray to black. This is seen in the first part of the range measurements from the black area. The raw range measurements fluctuate greatly until about half way through the area where they seem to steady out. This effect from changes in color only happens with dark gray to black objects. Changes from different colors of the lighter shades do not exhibit this trend.

4.8 Development of a Confidence Metric

In the previous sections, we developed a correction algorithm. It is also useful to know how much error is still present in the corrected data. By knowing how much error is still present in the data, we are able to derive a measure of confidence in the corrected data. Our definition of confidence is inversely proportional to the amount of error in the corrected range value. Our approach to this problem is to base the confidence value of the corrected range measurement only on the corresponding intensity value. This is because the relative error for all the distances are about the same. The relative error is

$$\mathcal{E}_r = \frac{|\mathcal{T} - \mathcal{R}_c|}{\mathcal{T}}, \tag{4.12}$$

where $\mathcal{T}$ is the ground truth value and $\mathcal{R}_c$ is the corrected range value. Figure 4.29 shows the relative error for four distances after our correction algorithm has been applied.

The first step is to calculate the squared error of the corrected range measurement. It is calculated by

$$\mathcal{E}^2 = |\mathcal{T} - \mathcal{R}_c|^2. \tag{4.13}$$

Ground Truth Distance (in)	*Mean of the Relative Error for the Corrected Range Values*
15	0.01173030
17	0.00767292
20	0.00700781
22	0.00459431

Figure 4.29: *Shows the relative error of the corrected range values for several distances. This confirms that the error is constant with respect to distance.*

We then plot $\mathcal{E}^2$ versus the experimental intensity. Figure 4.30 shows a plot of the squared error of the corrected range data for distances of 15, 17, 20, and 22 inches. The data was corrected by the fifth-order polynomial fit developed in the previous sections.

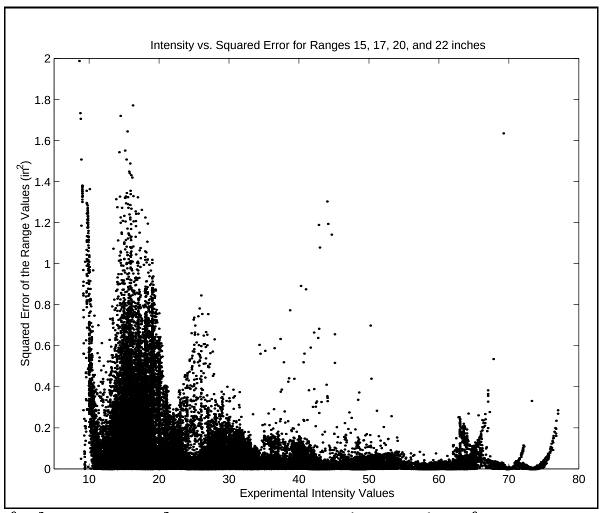

Figure 4.30: *A plot of the squared error versus intensity for range data taken at 15, 17, 20, and 22 inches.*

Now that we have the data, we fit a surface to it using the same method described in the previous sections. Part *(a)* of Figure 4.31 shows a third-order polynomial fit to the data shown in Figure 4.30. Notice how the latter part of the fit dips down below zero for higher intensity values. This is an undesirable effect caused by the method we used to fit the surface to the data. To eliminate this artifact, a threshold is used. For intensity values greater than 72, a squared error measurement of 0.005 in^2 is assigned to that intensity value. This number represents an average of the absolute squared error present for

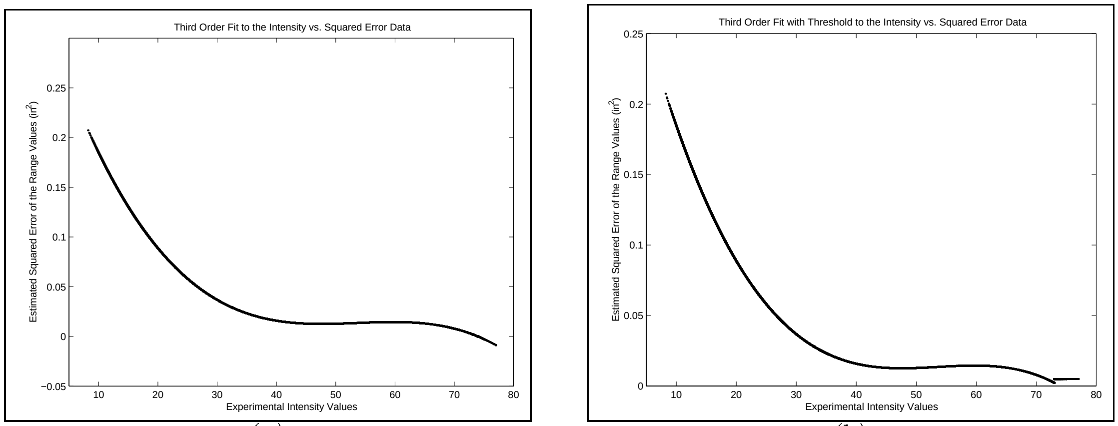

(a) *(b)*

Figure 4.31: *a) A third-order polynomial fit to the squared error of the data shown in the previous figure. b) The same polynomial fit with a threshold included to account for the negative values produced by our fit.*

intensity values greater than 72. Part *(b)* shows a plot of the fit with the threshold included.

Our confidence algorithm was applied to the stripe image taken at nineteen inches. Figure 4.32 shows the results. The confidence algorithm was also applied to the checkered board image taken at eighteen inches. Figure 4.33 illustrates the results. The images in both figures provide the intuitive information one would expect. The dark gray to black regions contain more error than the lighter shades. The magnitude of the expected error is also relatively close to the error obtained after correction.

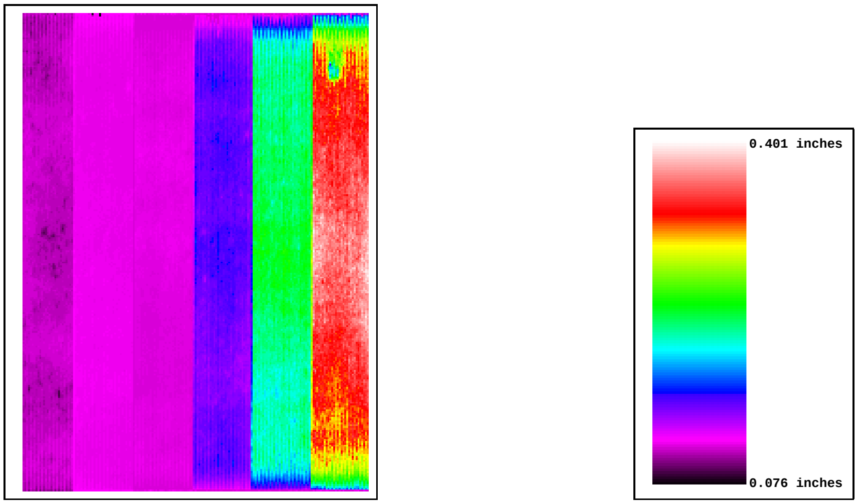

Figure 4.32: *Color-coded image of the confidence values for the stripe image taken at 19 in. along with the color-coded scale for the image.*

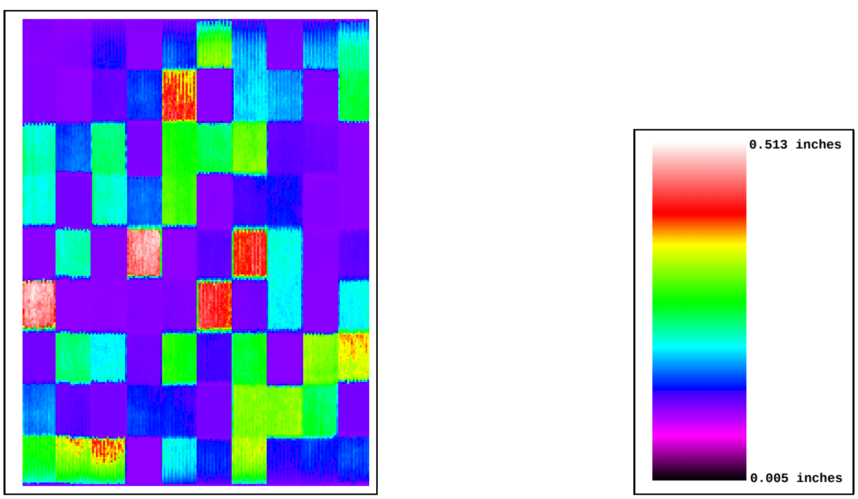

Figure 4.33: *Color-coded image of the confidence values for the checkered board image taken at 18 in. along with the color-coded scale for the image.*

CHAPTER 5

Conclusions and Future Work

We have constructed a versatile scanning system that is capable of acquiring data by several different methods with minimum rearrangement of operational parts. The system is divided into two aspects. The first being the data acquisition stage consisting of the AccuRange 3000 laser rangefinder. The second aspect of the system concerns the movement of the laser beam through out the region of interest. Both of these stages work seemlessly together to create our scanning system. All inputs into the system are described and entered into an input file that is read by the controlling program. This reduces the knowledge the user has to have to operate the system.

We have successfully identified and quantized all major sources of error present in the data acquisition phase of the system. From these errors, a correction algorithm has been developed that is capable of improving the accuracy and precision of the range measurements by at least fifty-five percent. To compliment the correction algorithm, we developed a confidence metric that is applied to the original data and produces an image that shows how much error can be expected in each range measurement after the correction process.

This thesis has demonstrated success in various aspects of our original goals, but there are areas that can be altered to yield better results. The first improvement can be made in the development of the correction algorithm. Early on in this project we made the assumption that temperature would be constant enough to achieve consistent range measurements. As it turns out, this was an incorrect assumption. We were able to prove that the temperature did not remain reasonably constant and showed the deviations in the range measurements as a result. Our correction algorithm was based on the experimental range and intensity values. It is clearly evident that temperature must be included to improve the accuracy of the correction algorithm.

Our choice of surface fitting algorithm was essentially a least squares minimization of an over constrained problem. This technique is known to have problems handling data not represented by the surface area. Points that were not represented in the original data set used to create the surface fit can cause the algorithm to produce erratic results. This is because the least squares minimization technique is a continuous function that becomes unstable at the boundaries of the surface. A possible better choice of a technique would be a noncontinuous function such as a b-spline. B-splines are known to be able to handle the problem of points lying outside the surface area.

In conclusion, we have obtained the goal set forth of error characterization and correction. Also, several areas of future development could improve the system by increasing its robustness and accuracy.

BIBLIOGRAPHY

BIBLIOGRAPHY

[1] D. Nitzan, "Three-dimensional vision structure for robot applications," *IEEE Transactions on Pattern Analysis and Machine Intelligence* **PAMI-10**, pp. 291–309, May 1988.

[2] G. A. Armstrong and G. R. Dochat, "Topographical Mapping System for radiological and hazardous environments acceptance testing," in *Proceedings of SPIE Conference on Intelligent Robots and Computer Vision*, vol. 3208, pp. 283–294, 1997.

[3] R. Baribeau and M. Rioux, "Influence of speckle on laser range finders," *Applied Optics* **30**, pp. 2873–2878, July 1991.

[4] Odetics, INC., *3–D Laser Imaging System User's Guide.*
Anaheim, CA, 1990.

[5] B. L. Chase, W. L. Green, and M. Abidi, "Range image acquisition, segmentation, and interpretation: A survey," tech. rep., Department of Electrical Engineering, University of Tennessee at Knoxville, 1995.

[6] P. J. Besl, *Active optical range imaging sensors*, pp. 1–53.
Springer-Verlag, 1988.

[7] M. I. Skolnik, *Introduction to radar systems*, McGraw-Hill, 1980.

[8] M. Koskinen, J. Kostamovaara, and R. Myllylä, "Comparison of the continuous wave and pulsed time-of-flight laser rangefinding techniques," in *Proceedings of SPIE Optics, Illumination, and Image Sensing for Machine Vision VI*, vol. 1614, pp. 296–305, 1992.

[9] M. Hebert and E. Krotkov, "3-D measurements from imaging laser radars: How good are they?," *IEEE/RSJ International Workshop on Intelligent Robots and Systems* , pp. 359–364, 1991.

[10] M. D. Adams and P. J. Probert, "The detection and removal of phantom range data from A.M.C.W. light detection and ranging sensors," tech. rep., Department of Engineering Science, University of Oxford, UK, 1996.

[11] I. S. Kweon, R. Hoffman, and E. Krotkov, "Experimental characterization of the Perceptron laser rangefinder," Tech. Rep. CMU-RI-TR-91-1, Carnegie Mellon University, 1991.

[12] R. Hoffman, S. Chheda, and C. Shepherd, "Improvement of laser rangefinder data through characterization," in *Proceedings of the ANS 7th Topical Meeting on Robotics and Remote Systems*, pp. 117–123, 1997.

[13] J. R. Davidson, "INEL testing of Perceptron LASAR^{TM} 3D camera system," tech. rep., Idaho National Engineering Laboratory, EG&G Idaho, Inc., 1994.

[14] R. Pito, "Characterization, calibration and use of the Perceptron laser range finder in a controlled enviroment," Tech. Rep. MS-CIS-95-05, Department of Computer and Information Science, University of Pennsylvania, 1995.

[15] R. E. Barry, M. Beckerman, B. E. Bernacki, T. W. Burgess, B. L. Burks, and O. H. Dorum, "A preliminary analysis of metrology techniques releated to ITER mapping requirements," tech. rep., Oak Ridge National Laboratory, 1994.

[16] K. S. Hashemi, P. T. Hurst, and J. N. Oliver, "Sources of error in a laser rangefinder," *Review of Scientific Instruments* **65**, pp. 3165–3171, October 1994.

[17] G. Champleboux, S. Lavallee, P. Sautot, and P. Cinquin, "Accurate calibration of cameras and range imaging sensors: The NPBS method," in *Proceedings of IEEE International Conference on Robotics and Automation*, vol. 2, pp. 1552–1557, 1992.

[18] M. Buzinski, A. Levine, and W. H. Stevenson, "Laser triangualtion range sensors: A study of performance limitations," *Laser Institute of America* **73**, pp. 1–15, 1992.

[19] X. Y. Jiang and H. Bunke, "Quantization error analysis in range sensing by active triangulation," tech. rep., Institut fur Informatik und angewandte Mathematik, Universitat Bern, 1993.

[20] S. Lang, L. Korba, F. Blais, and M. Lecavalier, "Characterization and testing of the BIRIS range sensor," *IEEE Instrumentation and Measurement Technology* , pp. 459–464, 1993.

[21] Y. D. Chen and J. Ni, "Dynamic calibration and compensation of a 3-D laser radar," *IEEE Transactions on Robotics and Automation* **9**, pp. 318–323, June 1993.

[22] R. Bajcsy, E. Krotkov, and M. Mintz, "Models of errors and mistakes in machine perception pt. 1," in *Image Understanding Workshop*, vol. 87, pp. 194–204, 1987.

[23] L. Matthies and P. Grandjean, "Stochastic performance modeling and evaluation of obstacle detectability with imaging range sensors," *IEEE Transactions on Robotics and Automation* **10**(6), pp. 783–792, 1994.

[24] S. Tamura, E.-K. Kim, R. Close, and Y. Sato, "Error correction in laser scanner three-dimensional measurement by two-axis model and coarse-fine parameter search," *Pattern Recognition* **27**(3), pp. 331–338, 1994.

[25] H. F. Durrant-Whyte, "Sensor models and multisensor integration," *International Journal of Robotics Research* **7**(6), pp. 97–113, 1988.

[26] Y. Kanazawa and K. Kanatani, "Reliability of plane fitting by range sensing," in *Proceedings of IEEE International Conference on Robotics and Automation*, vol. 2, pp. 2037–2042, 1995.

[27] M. A. Abidi and R. C. Gonzalez, eds., *Data Fusion in Robotics and Machine Intelligence*, Academic Press, Inc., 1992.

[28] R. R. Clark, "A laser distance measurement sensor for industry and robotics," *Sensors* **11**, pp. 43–50, June 1994.

[29] Y. Roth and R. Jain, "Simulation and expectations in sensor-based systems," *International Journal of Pattern Recognition and Artificial Intelligence* **7**(1), pp. 145–173, 1993.

[30] Y. Chen, G. Johnson, and D. Simon, "Fast complex surface inspection and verification using optical laser line scanner," *Transactions of the North American Manufacturing Research Intitution of Society of Manufacturing Engineers* **22**, pp. 247–252, May 1994.

[31] W. H. Press, S. A. Teukolsky, W. T. Vettering, and B. P. Flannery, *Numerical Recipes in C: The Art of Scientific Computing: Second Edition*, Cambridge University Press, 1992.

APPENDICES

APPENDIX A

Information on How to Use the Scanning System

This appendix describes how to use the scanning system developed for this thesis. It gives a description of which programs are needed to run the system and where they are located in the user account ~collier. Also, it describes how to compile the executable programs.

A.1 Point-by-Point Method

The point-by-point method turns the laser on and takes data at a point. The laser is then turned off and the stepper motors move to the next point where this process is repeated until the image is complete. The coordination of the taking of data and the moving of the laser is done by serial communication between vision22 and the PC known as "Pixel".

On the SGI side, I have written some code to handle the serial communication in class format. It is important to note that this and all other software written for the SGI is done on IRIX 5.3. The class source code for the serial communication program is in the directory

$$\sim collier/bin/SRC/CC/$$

An object file that can be included into the main point-by-point program is needed. The compile statement to produce the object file is

$$CC \quad -c \ port.cc$$

On the PC side, we are using *Borland C++* version 4.5. I have downloaded some serial communication software off of Borland's homepage that is very reliable and altered it to fit our needs. The file that contains the source code is called *Serial.C*, and it is in

$$C:/At6400/Samples/Tc20/$$

In order to use the software, just include the *.h* files for *Serial.C* in the main program.

Now that all the information about the serial communication has been discussed, a description of the main code will be given. The code that controls the low level SCSI communication for the Acuity laser is in

$$\sim collier/Acuity/gen\_soft/scsilib/$$

There are four main files in this directory. The first two are *acuity.c* and *range_u.c*. These files contain all of the class routines that communicate with the AccuRange SCSI interface. The other two files are *dslib.c* and *dstab.c*. These files contain the library routines for the SCSI device used by *acuity.c*. There is a makefile in this directory that makes all of the necessary files to be included in the main program (i.e. the object files).

The main controlling program for the point-by-point method is in the directory

$$\sim collier/Acuity/Point\_by\_Point/$$

The file *point.cc* is the main controlling program. It calls functions in the file *get_dist_P.c* to actually take the data. The compile statement for *get_dist_P.c* is

$$cc\ \ -c\ \ get\_dist\_P.c$$

The compile statement for *point.cc* is

$$CC\ \ -o\ \ point\ \ point.cc\ \ port.o\ \ get\_dist\_P.o\ \ range\_u.o\ \ acuity.o\ \ dslib.o\ \ dstab.o\ -lm$$

Point.cc reads information from a file called *inputfile*. *Inputfile* contains the operating parameters of the laser and information concerning the size of the image desired.

The program that coordinates with *point.cc* on the PC side is *Comm1.cpp*. It is in the directory

$$C : /At6400/Samples/Tc20/$$

To run the scanning system in the point-by-point mode there are several steps. First open the Borland interface on the PC and open the project titled $comm1.ide$. This loads the *Comm1.cpp* program into Borland. The second step is to run the program. This pops up a DOS window which allows the user to enter values for the length of travel for $stepper1$ and $stepper2$. The program then waits for a message from the SGI. The last step is to run the executable $point*$ on vision22. The system will automatically start taking data and moving the steppers. The data is taken in a serpentine manner.

This method produces a data file with all the information from the laser. I have written a program that will average all the samples taken per point and reorder the data into a raster scan sequence. The file is called $avg*$ and the source code for this file is in the directory

$$\sim collier/bin/SRC/REDO\_DATA$$

Avg.cc produces a data file that can be read by $fitimgr*$ or $ivimgr*$. These files create images from the data files. *Fitimgr.cc* creates a fit file and *ivimgr.cc* creates an inventor file of the data. The source code for $fitimgr.cc$ is in

$$\sim collier/bin/SRC/FITS$$

and the source code for *ivimgr.cc* is in

$$\sim collier/bin/SRC/REAL\_SYN\_IV$$

A.2 Line-by-Line Method

The line-by-line method turns the laser on and moves the beam the length of $stepper2$. While the beam is moving, the laser is acquiring data. The speed of data acquisition and the speed of stepper motor movement has been calibrated so the laser is taking data for almost the entire length of travel. The scanning region consists of a reflective mirror with a white matte surface in the center. Figure A.1 shows the setup previously described. The laser starts out in a high reflectivity area and moves across the white matte surface

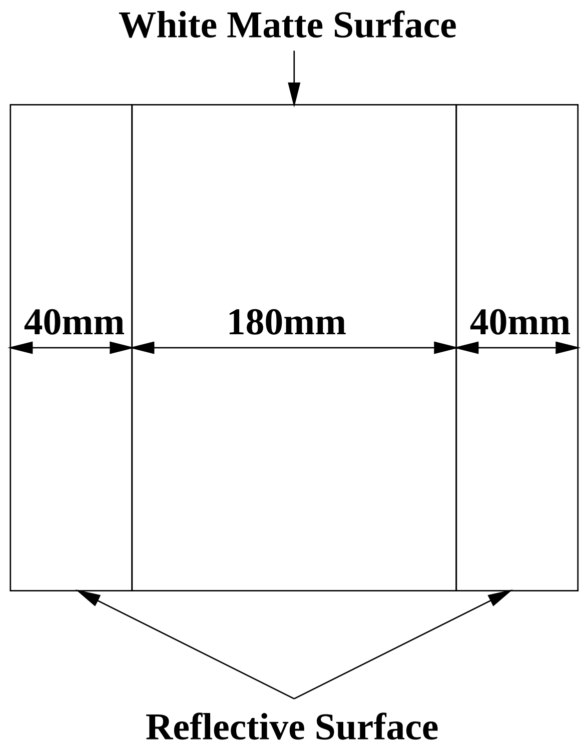

Figure A.1: *Reflective surface used to indicate region of interest for the line-by-line method.*

and back into a high reflectivity area. The program only outputs the data taken over the white matte surface.

The main controlling program for the line-by-line method is in the directory

$$\sim collier/Acuity/Line\_by\_Line/$$

The file *newline.cc* is the main controlling program. It calls functions in the file *get_dist_L.c* to actually take the data. The compile statement for *get_dist_L.c* is

$$cc \ \ -c \ \ get\_dist\_L.c$$

The compile statement for *newline.cc* is

$CC\ \ -o\ newline\ newline.cc\ port.o\ get\_dist\_L.o\ range\_u.o\ acuity.o\ dslib.o\ dstab.o\ -lm$

Newline.cc reads information from a file called *inputfile*. *Inputfile* contains the operating parameters of the laser and the information concerning the size of the image desired.

The program that coordinates with *newline.cc* on the PC side is *Comm2.cpp*. It is in the directory

$$C : /At6400/Samples/Tc20/$$

To run the scanning system in the line-by-line mode, open the Borland interface on the PC and open the project titled *comm2.ide*. This loads the *Comm2.cpp* program into Borland. Then run the program. This pops up a DOS window which is waiting for the SGI to send the data information concerning the length of travel for the stepper motors and the number of lines and samples. Next run the executable *newline** on vision22. The system will automatically start taking data and moving the steppers. The data is taken in a serpentine manner.

This method produces two data files with all the information needed to create an image. The two files are *output_laser.dat* and *numb_in_line.dat*. *Output_laser.dat* contains all the range data taken per line. *Numb_in_line.dat* contains the number of range measurements taken per line. I have written a program that reorders the data and scales the data. It then outputs the data to a file that can be used to form an image. This program is needed because the number of samples per line is not the same. The number of samples per line with the setup as is varies between 1235 and 1255. The program asks how many samples per line the user wants and does a weighted average of the samples to produce the desired number of samples. The program automatically reads in the two data files and produces another file called *reduced_samples.dat*. The file is called *wght_avg.cc*. The source code for this file is in the directory

$$\sim collier/bin/SRC/WGHT\_AVG$$

The compile statement for $wght\_avg.cc$ is

$$CC \;\; -o \;\; wght\_avg \;\; wght\_avg.cc \;\; array.o \;\; -lm$$

Once again, the programs $fitimgr*$ or $ivimgr*$ can be used to create a fit image or an inventor image from the data.

A.3 Using the Mirror

As mentioned in the thesis, the rotational system is not constructed but the software for the system is written. There is some minor changes that have to be made to the system. The five pin connector on the third from the left motor drive must be disconnected. The five pin connector from the rotational table is plugged in to the same place the other was removed. Also, the housing for the laser is different than for the other two methods. The laser and the mirror need to be connected to the other housing. This is rather simple because it only requires a few screws.

The overall structure of the hardware is similar to the previous two methods. The rotational table turns as the laser takes data using the mirror which forms the spherical scanning system. The rotational mirror has an encoder on it with about 2000 encoder values. These are *tick marks*. The laser takes data the entire time the mirror is spinning but only the data which falls between two predetermined tick marks is output to a data file.

The main controlling program for the mirror method is in the directory

$$\sim collier/Acuity/Mirror/$$

The file $mirror.cc$ is the main controlling program. It calls functions in the file $get\_dist\_M.c$ to actually take the data. The compile statement for $get\_dist\_M.c$ is

$$cc \ \ -c \ \ get\_dist\_M.c$$

The compile statement for $mirror.cc$ is

$$CC \ \ -o \ mirror \ mirror.cc \ port.o \ get\_dist\_M.o \ range\_u.o \ acuity.o \ dslib.o \ dstab.o \ -lm$$

$Mirror.cc$ reads information from a file called $inputfile$. $Inputfile$ contains the operating parameters of the laser and information concerning the size of the image desired.

The program that coordinates with $mirror.cc$ on the PC side is $Comm3.cpp$. It is in the directory

$$C : /At6400/Samples/Tc20/$$

To run the scanning system in the mirror mode, open the Borland interface on the PC and open the project titled $comm3.ide$. This loads the $Comm.cpp$ program into Borland. Then run the program. This pops up a DOS window which is waiting for the SGI to send the data information concerning the length of travel for the rotational table. Next run the executable $mirror*$ on vision22. The system will automatically start taking data and moving the rotational table. The data is taken in a raster scan manner. This method produces a data file that can be formed into an image by using the program $fitimgr*$ or $ivimgr*$.

VITA

Rick Collier was born in Irvine, KY in 1971. Shortly after he moved to Chicago, IL where he lived briefly until he moved to Paris, TN. He graduated from Henry County High School in May 1990 and received a scholarship to University of Tennessee at Martin. While at Martin, he studied electrical engineering and played collegiate baseball. In 1992, Mr. Collier transferred to the University of Tennessee at Knoxville where he completed his bachelors degree in electrical engineering in the Fall of 1995. In the Spring of 1996, he enrolled in the Masters program at the University of Tennessee at Knoxville as a Graduate Research Assistant in the Imaging, Robotics, and Intelligent Systems Laboratory under the tutelage of Dr. R. T. Whitaker and Dr. M. A. Abidi. Mr. Collier will graduate in the Summer of 1998 with a specialization in image processing and robotic vision.